4.2 Ground Penetrating Radar Data Acquisition -Drift Scale Test - to 07/22/01

4.2.1 Background:

The borehole radar method is one in which modified ground penetrating radar antennas are lowered into the ground and high frequency electromagnetic signals are transmitted through subsurface material to a receiving antenna. The electrical properties of the subsurface material, here the repository rock, influence the properties of the transmitted electromagnetic signal. In particular, the dielectric permittivity of the rock has a strong influence on the propagation of the signal and whether it travels at a high or low velocity or whether it is highly attenuated or not. Moisture content has such an effect. The high dielectric permittivity of water - in contrast to dry rock - typically results in greatly reduced signal velocities and increased signal attenuation. It is such changes in signal character that are to be measured over the course of the Drift Scale Test. Additionally, the transmitted signals may be represented as multiple raypaths crossing through the zone of interest. If sufficient raypaths are recorded, a tomographic image may be obtained through computer processing. The information extracted from such data includes the following: a) the transit time which depends on the wave velocity, and b) the amplitude which depends on the wave attenuation. This information, in the form of a processed tomogram, offers a high-resolution approach to monitoring the changes occurring in the repository rock over the duration of the thermal experiment.

All field measurements were performed by qualified personnel, with calibrated equipment, under the LBNL QA program. Therefore, all data presented in this report are qualified data.

4.2.2 Equipment Description:

All radar data were acquired using the Sensors and Software pulseEKKO 100 ground penetrating radar system equipped with 100 MHz center frequency borehole antennas. The pulseEKKO system consists of six basic components, including a pair of identical antennas, a transmitter electronics unit, a receiver electronics unit, a control console and a personal computer acting as a recording system and data storage unit.

Antenna Specifications -
The pulseEKKO 100 antennas are resistively damped dipolar antennas. The antenna radiation patterns are the pattern of a half wavelength dipole. Each antenna pair is designed to have a bandwidth to center frequency ratio of one. The borehole antennas used in the Drift Scale Test have a center frequency of 100 MHz.

Transmitter Electronics Specifications -
The pulseEKKO system used in the Drift Scale Test consisted of a 1000 volt transmitter having a peak voltage of 1000 volts with fa rise time of 2.5 nanoseconds. The transmitter is powered by 12 volts and emits a pulse on command from the control console. The power actually radiated from the system is very dependent on the subsurface conditions.

The 1000V transmitter used here delivers a peak power of 3.2 kilowatts into a 50 ohm load. Only a small fraction of the available power is actually transformed into a radiated electromagnetic signal because the antennas are damped and are very inefficient radiators.

Receiver Electronics Specifications -
The receiver electronics digitize the voltage at the receiver antenna connector to 16-bit resolution. The receiver design is such that it acquires the received waveform with very high fidelity. The receiver electronics clip the incoming voltage at a 50 mV level and the receiver noise level is nominally around 200 microvolts per stack. The present receiver resolution for a single bit after analog to digital conversion is 1.5 microvolts.

Control Console -
The control console provides the overall management of the transmitter and receiver operation. The control console is a microprocessor controlled unit which communicates with both the transmitter and receiver electronics and the external PC. The PC passes the system configuration information and the acquisition parameters to the control console which then manages all of the hardware functions of the PulseEKKO radar system.

4.2.3 Operating Principles:

The operating principles were as follows:
a) the user defines the time window, sampling interval and number of pulses to be stacked via the PC user interface; b) the user selects the acquisition mode; c) the PC configures the pulseEKKO console through the PC's standard RS232 port and the console takes over control of data acquisition; d) the pulseEKKO console commands the transmitter to fire; the transmitter generates a high voltage pulse which is shaped by the transmitting antenna into a radiated pulse; e) the console advises the receiver electronics to digitize the signal from the receiving antenna; the receiver digitizes the ambient electric field present at the receiving antenna after the band limiting characteristics of the antenna transfer function; the digital number representing the voltage at the time of acquisition is transferred to the control console; f) steps d) and e) are repeated until the desired waveform length and stack count are achieved; g) the console transmits the stacked waveform to the PC; h) the PC stores the data and displays the radar trace.

4.2.4 Survey Methodology:

The borehole radar technique utilized is a crosshole radar profiling method in which the transmitter and receiver antennas are located in separate boreholes and data are collected with the antennas at various vertical offsets. Data are collected using two acquisition modes. The first is a Zero Offset Profile (ZOP) in which measurements were taken with the transmitting and receiving equidistant down the two boreholes. The second is a Multiple Offset Profile (MOP) in which the receiving antenna remained at a fixed location while the transmitting antenna is moved incrementally in the second borehole. It is a series of multiple offset profiles that are to be used to acquire the raypaths necessary for subsequent tomographic processing.

The radar data are acquired in ten boreholes orthogonal to the primary direction of the Heated Drift. The boreholes are accessed from the Access Observation Drift and are the same boreholes used in the neutron data acquisition. The ten boreholes include the following:

Borehole No.:	Borehole ID:
47	ESF-HD-NEU-1
48	ESF-HD-NEU-2
49	ESF-HD-NEU-3
50	ESF-HD-NEU-4
51	ESF-HD-NEU-5
64	ESF-HD-NEU-6
65	ESF-HD-NEU-7
66	ESF-HD-NEU-8
67	ESF-HD-NEU-9
68	ESF-HD-NEU-10

The location of these boreholes needs to be precisely determined in order for the radar data to be accurately processed. All positions along the length of the borehole where data are collected need to be determined. The convention for the Drift Scale Test as-built coordinates is that the origin (0,0,0) is at the center of the Heated Drift on the hot side of the bulkhead, the +Y-axis is along the Heated Drift which parallels the Access Observation Drift toward the west, the +X-axis runs to the north away from the Access Observation Drift, and the +Z-axis is upward. The as-built survey coordinates (DTN: LANE834244AQ97.001) provide collar, bottom-hole and several intermediate points between collar and bottom hole for each borehole in the Drift Scale Test - including those used in radar data acquisition. Because many boreholes in the Drift Scale Test are beyond the line of sight and the bottom hole coordinates provided by the survey data (DTN: LANE834244AQ97.001) are in fact projected by the surveyors, the thermal testing team has reevaluated all of the surveyed boreholes, with regards to the straightness of each borehole, and the reliability of the projected bottom hole coordinates. This effort resulted in some modification of the as-built survey data contained in (DTN: LANE834244AQ97.001); and these modifications are now contained in a separate TDIF (DTN:MORW831213DQ98.001). All of the radar data borehole coordinates are based on the collar and bottom hole coordinates contained in this latest TDIF (DTN:MORW831213DQ98.001).

The first order results derived from the radar data are travel times and the resulting velocities. To determine accurate travel times between the transmitter and receiver antennas, it is vital to know the precise time at which the transmitter fires (known as time-zero). The procedure used to determine time-zero for the surveys consisted of taking four direct air wave measurements (the signal from transmitting antenna to receiving antenna in air) with the antennas held in air at a separation of 2.0 meters. After the time-zero data are collected, the antennas are immediately moved into the boreholes and a ZOP dataset is collected, concluding with another set of four measurements in air at 1.5

meter separation. Following this procedure, the MOP datasets were collected with the locations determined before the start of the survey. The transmitter and receiver intervals were every 0.25 meters. As in all MOP gathers, the receiving antenna remained at a fixed location (1m, 1.25m, 1.5m, etc.) while the transmitting antenna occupied each of its possible locations along the length of the borehole (e.g., 0-35.0m at 0.25m spacing). In this manner, all MOP gathers are collected and sorted as receiver gathers with filenames corresponding to the well pair being surveyed and the fixed receiver location (e.g., MOP10400 - an MOP gather collected for well pair #1 at a receiver location 4.00m below the wall surface). In this manner, each of the necessary raypaths was collected and recorded for the subsequent tomographic processing. Following MOP acquisition, a final ZOP dataset is collected as described above. This is done in an attempt to estimate any time-zero drift that may have occurred during the course of the survey. By comparing the two ZOP datasets along with the identical data included in the MOP dataset, any time-zero drift may be compensated for and corrected. This is discussed in more detail below.

Radar data were collected in this manner between the ten boreholes resulting in a total of eight well pairs. The well pairs include the following (referenced by Borehole Number): 47-48, 48-49, 49-50, 50-51, 64-65, 65-66, 66-67, and 67-68. The severity of the borehole inclination in the well pairs 47-48 and 64-65, however, limited the data acquired between these boreholes to ZOP data only. Full MOP data coverage could not be accomplished. These well pairs represent data coverage that is far enough away from the Heated Drift intersection that the loss is not expected to be severe.

4.2.5 Date Acquisition

GPR data have been acquired according to the following schedule:

Acquisition	Date	Days from heater initiation	Well Pairs
PRE	10/29/97	-33.00	51-50, 50-49, 68-67, 67-66, 66-65
PHASE 1	02/13/98	74.00	51-50, 50-49, 68-67, 67-66, 66-65
PHASE 2	01/26/99	421.00	51-50, 50-49, 68-67, 67-66, 66-65
PHASE 3	04/15/99	533.00	51-50, 50-49, 68-67, 67-66, 66-65
PHASE 4	10/26/99	694.00	51-50, 50-49, 68-67, 67-66, 66-65
PHASE 5	04/13/00	864.00	51-50, 50-49, 68-67, 66-65
PHASE 6	09/28/00	1032.00	51-50, 50-49, 66-65
PHASE 7	02/06/01	1163.00	51-50, 50-49, 66-65

After acquisition Phase 1, the borehole temperatures became so great that the cables used in the measurements melted. It took almost a year to design and manufacture cables that were more heat resistant. During acquisition Phase 5, the temperature in borehole 67 was so high that it caused stretching of the cable so that accurate measurements could not be taken.

Over the course of the heater experiment, the radar system was operated by using identical acquisition parameters for each of the field surveys. No adjustments, filters or gains are applied to the stored raw data. Therefore, data acquisition and hence data repeatability is the same regardless of who operates the system and when - so long as the antenna configuration is the same. Data repeatability is tantamount to successful tomographic differencing and interpretation. Small deviations in experimental methodology at such close spacing can result in large discrepancies in data processing.

Travel time tomography uses the first arrival times picked from the recorded MOP waveforms for each transmitter-receiver pair to obtain an estimate of the two-dimensional interwell velocity structure based on an inversion algorithm. The inversion method is based on the relation between propagation velocity and the total travel time along a ray path between a transmitter and receiver:

$$T = \int_R u(\boldsymbol{r})dl \qquad (1)$$

where T is the travel time, $u(\boldsymbol{r})$ is the slowness, or inverse velocity, at a coordinate in space $\boldsymbol{r}$ and dl is the incremental distance along the raypath with total length R. When inverting the travel times for slowness, the region of interest is generally divided into cells of constant slowness. Under these discretized conditions, Eq. 1 can be described by a set of linear equations

$$t_k = \sum_{i=1}^{N} u_i l_{ki} \qquad (2)$$

where t_k is the travel time of the kth raypath, u_i is the slowness estimate of the ith cell, l_{ki} is the length of the kth raypath in the ith cell, and N is the total number of cells. An Algebraic Reconstruction Technique (Peterson et al., 1985) is used in the travel time inversion for velocities.

4.2.6 Measurement error

There are two types of measurement error that can occur: errors in antenna location done the borehole and zero time error. In order to determine accurate travel times between the transmitter and receiver antennas, it is necessary to know the zero time, which is the precise time in the recorded signal when the transmitter fired. The zero time (if not at the start of the recording) must be subtracted from the measured travel times to obtain an accurate absolute first arrival time of the electromagnetic wave. An accurate method of determining the zero time is to simply record a travel time, t_i, over a precise distance between the antennas in air at one offset, x_i, usually approximately two meters in distance. The travel time of radar waves (t_c) for this offset is calculated by dividing the offset distance, d_i, by the electromagnetic wave velocity in air, $t_c = \frac{d_i}{3.0 \times 10^8 \ m/s}$. For a two meter offset, t_c = 6.66 ns. This calculated time is then subtracted from the measured travel time for this offset, $t_0 = t_i - t_c$, and the remainder is the zero time. Again, subtraction of t_0 from all the picked travel times yields the absolute travel times.

Compensation for zero time following the above procedure is sometimes not sufficient due to significant zero time drift which can occur at any time during crosswell data collection. A method of checking the behavior of the zero time drift is to compare Zero Offset Profile (ZOP) travel times, collected before and after crosswell data with coincident zero offset travel times extracted from the crosswell (MOP) data set. If the travel times for all three data sets coincide, then the zero time did not drift. If the two ZOPs do not coincide, then a zero time drift has occurred. Observation of the behavior of the zero time drift can indicate how the MOP travel times deviate from one ZOP travel time curve to the other. Figure 88 provides an example of these three travel time data sets during acquisition of one well pair. This illustrates how zero time drift is checked for and also illustrates the repeatability of the antenna location down the borehole. The average difference in travel time for these three data sets is about 0.2 ns, or about 0.4% of the travel time. Figure 89 illustrates a single ZOP curve from each of the 8 acquisition times from borehole pair 5-4. This shows the repeatability of the measurements (assuming little velocity changes between source numbers 20 and 60) during the 3 year acquisition time span.

4.2.7 Saturation calculations

Matrix saturation can be determined from radar velocities. Radar velocities are converted to bulk dielectric constant through the equation: $\kappa_B = \frac{c^2}{v^2}$ where:

$\kappa_B \equiv$ Bulk dielectric constant
$c \equiv$ velocity of electromagnetic waves (3.0×10^8 m/s)
$v \equiv$ velocity of electromagnetic waves in the material

A mixing formula is then used to determine the matrix saturation for a given porosity. The mixing formula can be written:

$$\sqrt{\kappa_B} = \varphi(1 - S_W)\sqrt{\kappa_a} + \varphi S_W \sqrt{\kappa_W} + (1 - \varphi)\sqrt{\kappa_m}$$

where:

$\kappa_B \equiv$ Bulk dielectric constant (get from velocity tomogram)
$\kappa_m \equiv$ Matrix dielectric constant
$\kappa_W \equiv$ Water dielectric constant (=81)
$\kappa_a \equiv$ Air dielectric constant (=1)
$S_W \equiv$ Saturation
$\varphi \equiv$ porosity

Solving for saturation:

$$S_W = \frac{\sqrt{\kappa_B} - \varphi\sqrt{\kappa_a} - (1-\varphi)\sqrt{\kappa_m}}{\varphi(\sqrt{\kappa_W} - \sqrt{\kappa_a})} = \frac{\sqrt{\kappa_B} - \varphi - (1-\varphi)\sqrt{\kappa_m}}{8.0\varphi}$$

Assuming the matrix dielectric constant is a constant 6.7 (determined from laboratory data):

$$S_W = \frac{\sqrt{\kappa_b} - 1.59\varphi - 2.59}{8.0\varphi}$$

It is evident from this equation that a porosity value is needed to calculate the saturation. Initially, it was decided that the baseline radar measurements would be used to calculate the porosity for each radar velocity cell using the inverse of above equation with a constant saturation of .80. For subsequent acquisitions, the saturation was calculated for each radar velocity cell using the above equations with the calculated baseline porosity values. These saturation values were subtracted from the baseline value of 0.80 to determine the change in saturation between the two acquisition times.
The saturation values calculated in this manner are subject to several assumptions and errors. There are inversion errors from the calculation of the bulk dielectric constant (κ_B); Errors due to the assumption of a constant saturation value of 0.80 used in the initial porosity value calculation; and Errors produced from the mixing formula, due to improper values, and the inaccuracy of the formula itself. Because of these inaccuracies, the change in water content is now calculated instead of the change in saturation. All values after July 2001 will be change in water content.
Water content is defined as saturation times
porosity ($S_W\varphi$), thereby removing the need to determine both of these values. Water content is also the parameter measured by the neutron probe, so comparison with those measurements will be easier. The change in water content can be calculated by subtracting the baseline saturation measurements:

$$S_{W0} = \frac{\sqrt{\kappa_{B0}} - \varphi - (1-\varphi)\sqrt{\kappa_m}}{8.0\varphi}$$

from measurements taken after heater initiation:

$$S_{W1} = \frac{\sqrt{\kappa_{B1}} - \varphi - (1-\varphi)\sqrt{\kappa_m}}{8.0\varphi}$$

$$\varphi(S_{W1} - S_{W0}) = \frac{\sqrt{\kappa_{B1}} - \sqrt{\kappa_{B0}}}{8.0}$$

where $\varphi(S_{W1} - S_{W0}) \equiv$ Water Content
Only inversion errors are contained in this calculation. However, it is not possible to determine an absolute value of water content unless a baseline value is assumed. The

water content calculation is as accurate as the inversion itself. The saturation calculation produces an absolute value, though it will have more errors.

4.2.8 Results

Previously, the data have been processed to give tomograms of liquid saturation as discussed in previous reports. The data are now processed to give the change in water content, as shown in Figures 90 and 91. Since the change in water content is now calculated, a complete set of difference tomograms is included here. It is clear from the figures that the largest regions of drying, which surround the wing heaters and the area closest to the Heated Drift, are increasing in size and becoming more dry for each acquisition time. However, the rate of drying slows in the later acquisitions. The distribution of moisture continues to corroborate well with other Drift Scale Test data, such as the neutron probe data and ERT data. These drying and wetting zones are also consistent with the predictions from the thermal-hydrological models. Based on the observations above, it appears likely that the GPR data continue to provide a useful representation of the conditions currently present in the rock mass surrounding the Drift Scale Test.

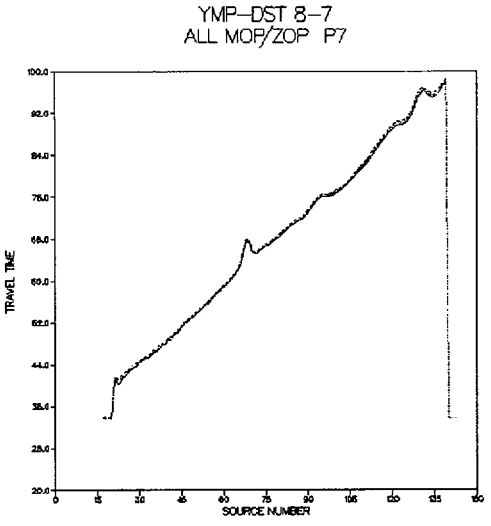

Figure 88 Example of Three Travel Time Data Sets During Acquisition of One Well Pair

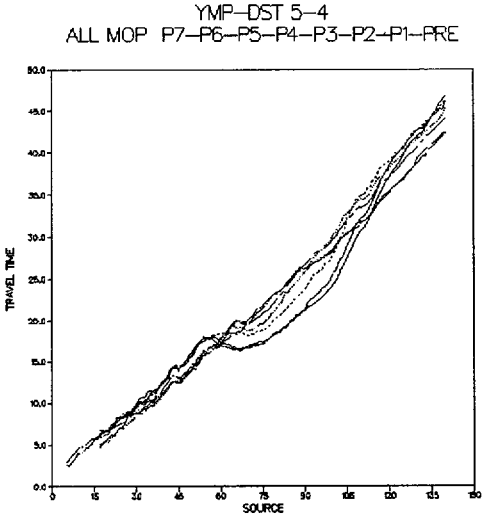

Figure 89 Single ZOP Curve from Each of the 8 Acquisition Times from Borehole Pair 5-4

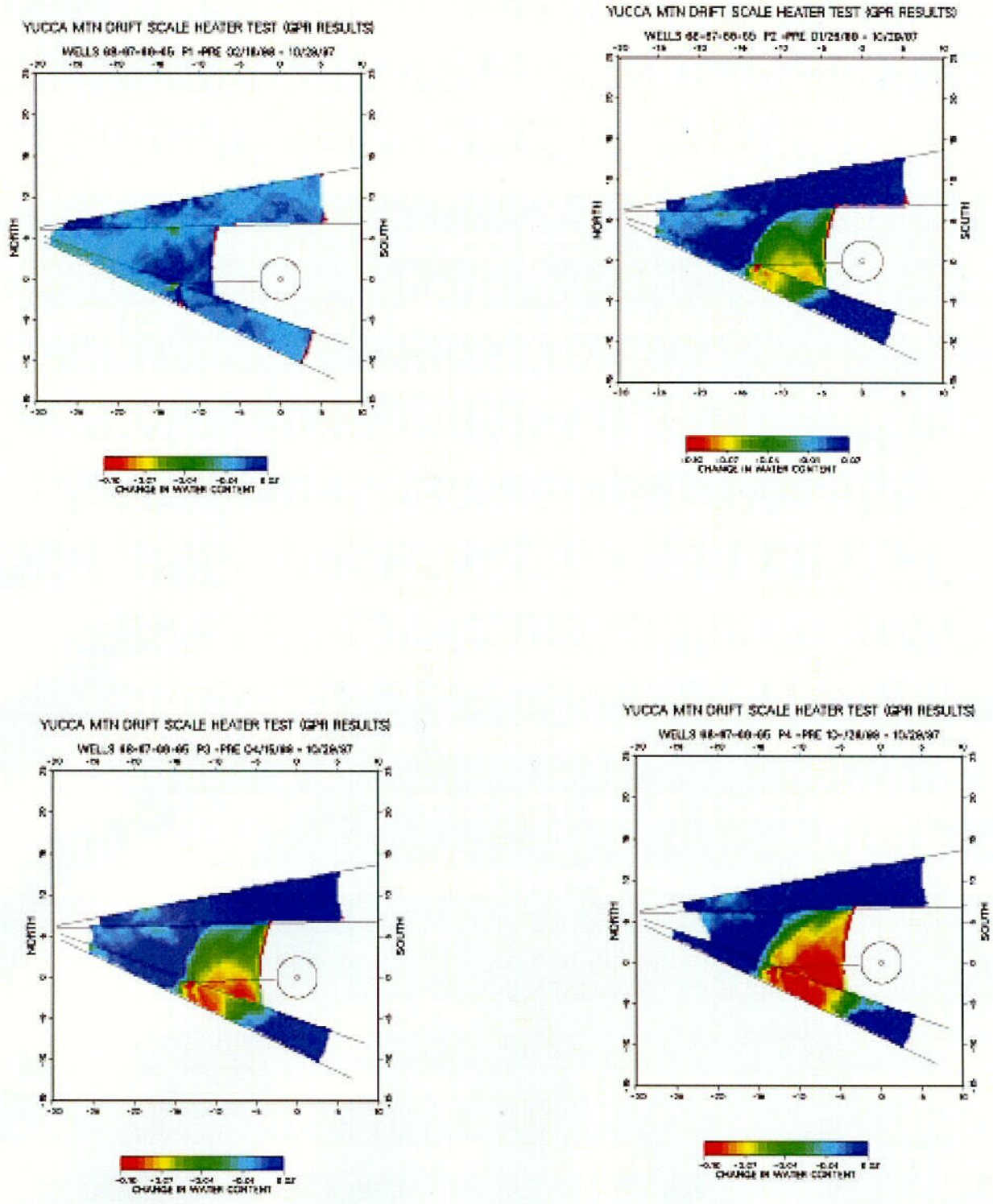

Figure 90. Change in water content for wells 68-67-66-65 for the four post heater acquisition times.

C01

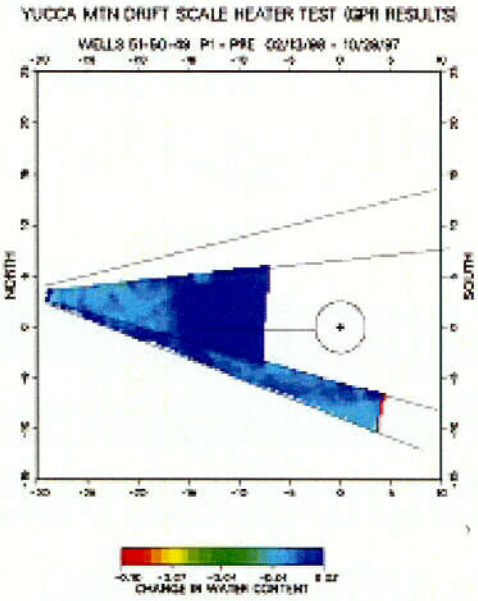
YUCCA MTN DRIFT SCALE HEATER TEST (GPR RESULTS)
WELLS 51-50-49 P1 - PRE 02/13/98 - 10/28/97
NORTH
SOUTH
-30
-25
-20
-15
-10
-5
0
5
10
-0.10
-0.07
-0.04
-0.01
0.02
CHANGE IN WATER CONTENT

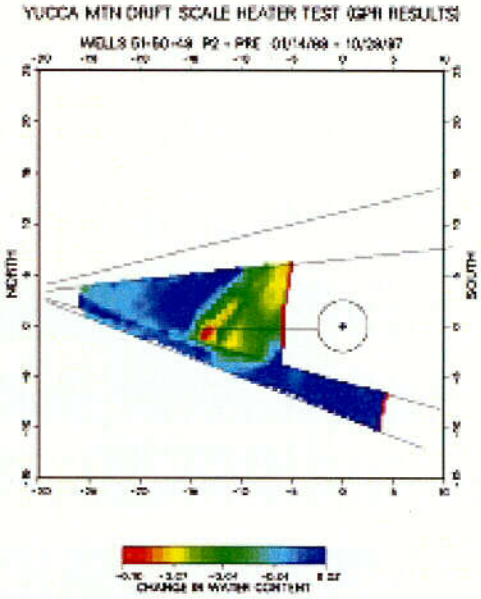
YUCCA MTN DRIFT SCALE HEATER TEST (GPR RESULTS)
WELLS 51-50-49 P2 - PRE 01/14/99 - 10/28/97
NORTH
SOUTH
-30
-25
-20
-15
-10
-5
0
5
10
-0.10
-0.07
-0.04
-0.01
0.02
CHANGE IN WATER CONTENT

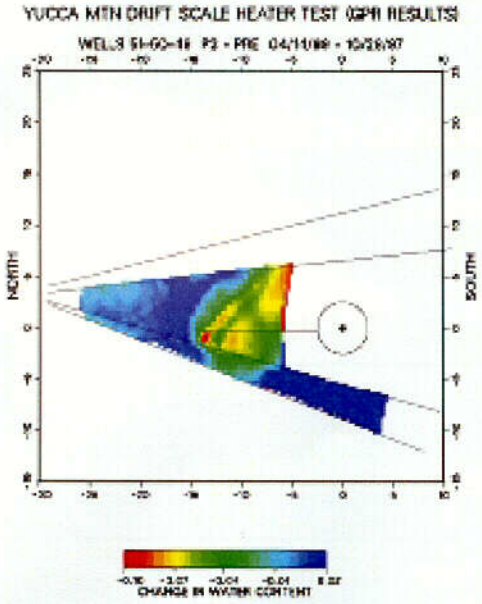
YUCCA MTN DRIFT SCALE HEATER TEST (GPR RESULTS)
WELLS 51-50-49 P3 - PRE 04/11/99 - 10/28/97
NORTH
SOUTH
-30
-25
-20
-15
-10
-5
0
5
10
-0.10
-0.07
-0.04
-0.01
0.02
CHANGE IN WATER CONTENT

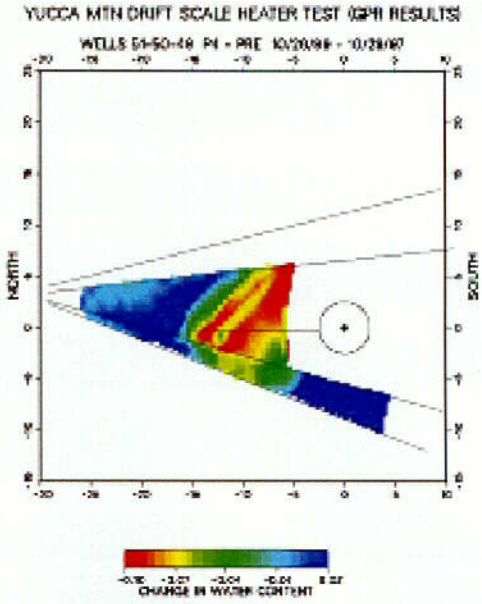
YUCCA MTN DRIFT SCALE HEATER TEST (GPR RESULTS)
WELLS 51-50-49 P4 - PRE 10/20/99 - 10/28/97
NORTH
SOUTH
-30
-25
-20
-15
-10
-5
0
5
10
-0.10
-0.07
-0.04
-0.01
0.02
CHANGE IN WATER CONTENT

C02

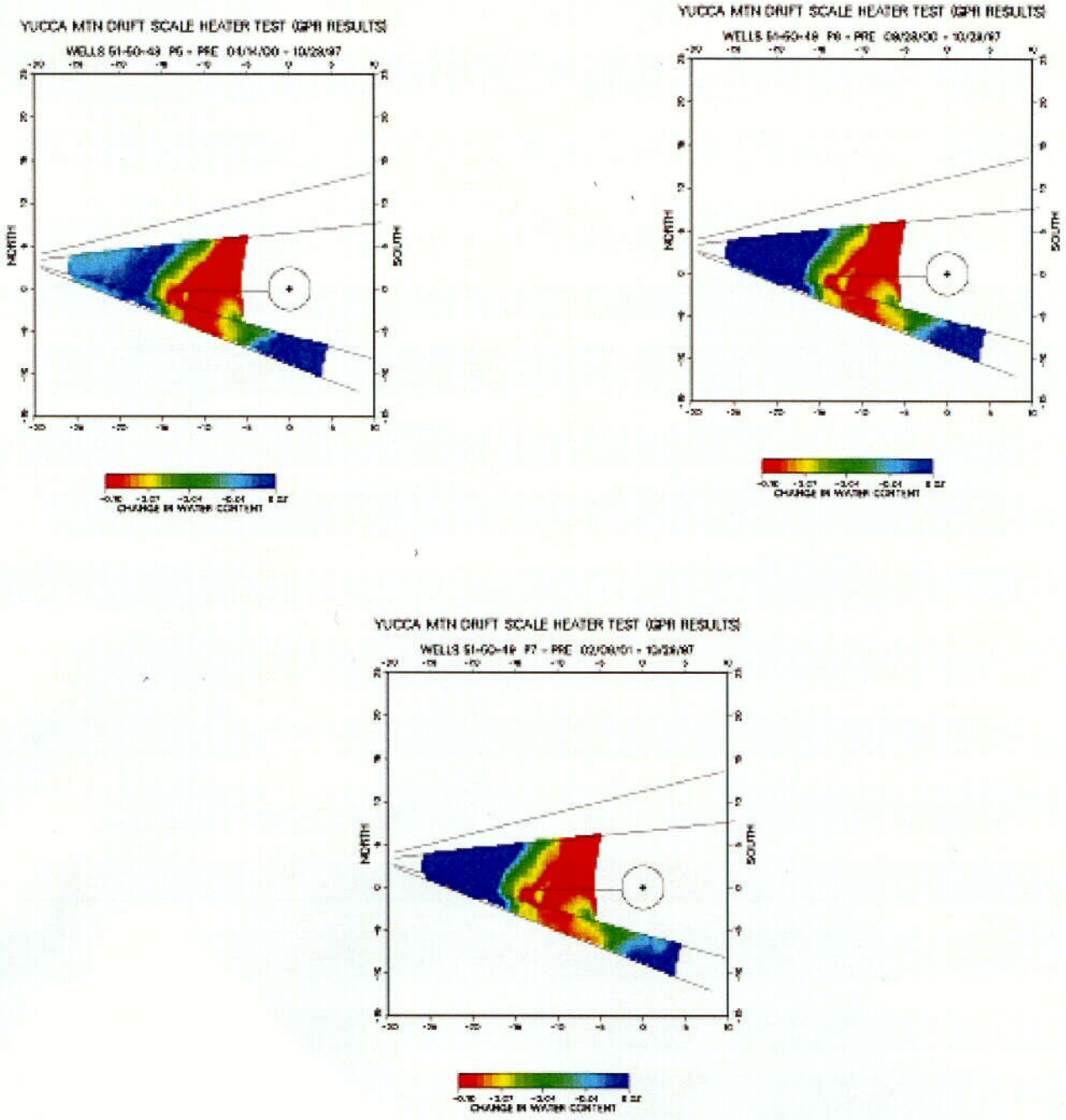

Figure 91. Change in water content for wells 51-50-49 for the seven post heater acquisition times.

C03

4.3 Thermal-Hydrological Model Validation: Integrated Assessment of Measurements and Comparison with Model Results

4.3.1 Introduction

Data used for tracking thermal-hydrological processes are the spatial and temporal evolution of (1) temperature and (2) moisture redistribution. Thermal-hydrological (TH) coupling is reflected in temperature readings that remain at the nominal boiling temperature of ~ 97 °C, resulting from two-phase conditions. Periodic geophysical logging by electrical resistance tomography (ERT), ground penetrating radar (GPR) crosshole tomography, and neutron logging are all tools for evaluating liquid saturation changes in the matrix, where the majority of liquid water resides. As fractures are mostly drained of water at ambient conditions, the fracture pore space is essentially air-filled. Periodic air permeability measurements therefore specifically target liquid saturation changes in the fractures.

The YMP thermal test program for the Drift Scale Test (DST) follows the approach of close integration between modeling and measurements. This involves

(1) Pre-heat characterization of site specific properties important for coupled processes (e.g., measurements of matrix saturation and fracture permeability for thermal hydrological processes). These measured parameters are used as model input for the DST.
(2) Predictive numerical modeling prior to the commencement of the actual test.
(3) Using the early test results (from the first few months of heating) to discriminate between alternative conceptual models applied in pre-test simulations.
(4) Continued interpretative analysis of measurements, refining the numerical model as and when needed.

Following this approach, the 3-D TH model for the DST was frozen without any refinement since the first progress report on the DST [CRWMS M&O 1998; Tsang et al., 1999]. Then, at 30 months of heating (September 2000), one modification to the TH model was made. The modification consisted of assigning those numerical gridblocks that contain wing heaters a fracture permeability several orders of magnitude higher than that of the rock. This is different from the prior conceptual model, in which gridblocks containing the wing heaters were assigned the same rock properties as the rest of the test block. Unless stated otherwise, simulated results presented in this current progress report (# 7) will be based on the conceptual model that includes this latest modification.

4.3.2 Comparison of Measured Temperature Data with Numerical Model Predictions

Illustrations of temperature signatures that reflect thermal hydrological coupling are presented in Figures 92 through 94. These show the temperature profiles along the eight boreholes 137 –144 at 33, 36, and 39 months of heating, respectively. The plots for the measured temperatures are on the left; and the plots from simulations are on the right. For boreholes 139 and 143, both the data and simulations show a temperature plateau at

nominal boiling temperature of ~ 97°C at about 15 meters from the collar. Boreholes 139 and 143 are horizontal boreholes parallel to the wing heaters. The temperature plateau for these boreholes is a signature of drainage of condensate water just beyond the outer edge of the wing heaters. Figures 92 through 94 also indicate another set of temperature plateau at ~ 97 °C, located between 6 to 12 meters from the collar of the boreholes at the Heated Drift. This set of temperature plateaus indicates a two-phase zone immediately outside the dry-out region surrounding the Heated Drift. Since the volume of drying continues to increase with heating, this two-phase zone would move out and away from the Heated Drift with time. At 12 months of heating, this set of temperature plateau was located at around 2 to 4 meters from the collar.

While Figures 92 – 94 show temperature profiles at specified times during the heating phase, comparison between measured and simulated temperature can also be displayed in the temperature history of selected sensors at specified locations. Figure 95 shows such a comparison for a number of sensors along one of the horizontal boreholes above the wing heater, borehole 160. In this borehole, Sensor 3 is within 1 meter of the borehole collar, Sensors 9 and 17 are above the inner wing heater, and Sensors 44 and 55 are beyond the edge of the outer wing heater. The measured data are shown on the left (sharp dips in the data correspond to power outages), and the simulated temperatures for the respective sensors are shown on the right. Note again the plateaus at the nominal boiling temperature of 97°C, indicating two-phase regions from TH coupling. For those sensors in close proximity to the heat source (Sensor 3 is closest to the Heated Drift, and Sensors 9, 17, 23, 33 are parallel to and only slightly above the wing heaters) these two-phase phenomena occur early, within the first few months of heating, and for short periods of time. The plateau for Sensor 44 occurs much later (starting at ~15 months of heating) and lasts for a longer duration. The temperature registered by this sensor exhibits the shedding of water beyond the outer edge of the wing heaters.

To assess how well the 3-D numerical model can predict the TH processes in the DST, mean error and root mean square error between the simulated and the measured temperatures in ~1700 temperature sensors were computed at specified times. These temperature sensors are installed in 26 boreholes in five radial arrays emanating from the Heated Drift. Table 2 shows a typical statistical comparison between modeled and measured temperature data, starting at 3 months and ending at 39 months of heating. Statistics for simulations for two alternative conceptual models of the heater boreholes are presented up to 18 months of heating. The values in the second and third columns in Table 2 are based on the conceptual model in which the gridblocks containing the wing-heater boreholes are assumed to have the properties of the rock. The values in the fourth and fifth columns in Table 2 are derived from the conceptual model, where to account for the open wing-heater boreholes, the gridblocks containing them are assigned fracture permeability several orders of magnitude higher than that of the rock mass. Statistics for this latter conceptual model was computed up to the more-recently measured data at 39 months of heating.

Observe that the mean error between simulated and measured temperatures in Table 2 is mostly positive, indicating that the simulations on the whole predict more heat being

retained in the rock than in the actual test. Table 2 also shows that the mean errors for the conceptualization in which the wing heaters are treated as high-permeability conduits are considerably smaller than that in which the wing-heater gridblocks are given the same property as that of the rock in the test block. This is because when the wing-heater grid-blocks are treated as high-permeability conduits, they act as preferential paths for the vapor generated from boiling. As a result, more vapor is transported through the wing heater boreholes and the Heated Drift out to the cool side of the bulkhead. The vapor leaving the bulkhead carries with it the latent heat of condensation, constituting the dominant source of heat loss from the test. Therefore, larger vapor loss results in smaller mean error in Column four. Larger vapor loss also implies that less condensate water is retained in the test block.

Figure 96 shows how the two conceptual models give rise to different TH temperature signatures, illustrating conceptual model uncertainty. Figures 96a and 96b show the temperature contours for the array of boreholes 158 –165 at 12 months of heating for the two alternative conceptual models of the wing heaters: (a) modeled as rock and (b) modeled as high-permeability conduits. Because the latter predicts more vapor loss (resulting in less condensate water being retained in the test block), the heat-pipe signatures are of much shorter duration in (b) than in (a). The measured data are shown in (c).

4.3.3 Comparison of Periodic Measurements of Moisture Redistribution with Model Predictions

The condensed water from the vapor is redistributed in the rock mass. Presently, zones of increased and decreased water content (from preheat baseline) are being monitored in the DST by periodic geophysical measurements and air-permeability measurements. These methods are useful for assessing qualitative changes, but do not give direct and reliable measured values for the absolute liquid saturation/moisture content of the matrix and fractures. Therefore, for validating the conceptual processes that control this moisture distribution, we do not attempt to match numbers from the measurements to our simulations, as in the case of temperature discussed earlier. Rather, the trends in the data for particular locations in the test are the most useful observations for model validation.

Air-Permeability Measurements

Periodic air injection test are performed in the 12 hydrology boreholes to assess (primarily) the wetting and drying in the fractures. Wetting of fractures means increase resistance to air flow during air-injection tests, leading to a decrease in air permeability from its preheat value.

These permeability data are used to validate the process model in the following manner. Simulated fracture liquid saturation contours at different phases of heating are generated in the three planes of the 12 hydrology boreholes. Then the measured permeability values are compiled and correlated to the simulated fracture saturation. To do this, the measurements are taken quarterly in different borehole locations, with each normalized to its preheat value. It is observed that for those borehole sections situated in zones of

increased liquid saturation (as predicted by the numerical model), the measurement displays a trend of decreased permeability. As heating progresses and the drying around the Heated Drift and the wing heaters expands, certain borehole sections that were previously zones of increased liquid saturation would become zones of decreased liquid saturation.

As an illustration, Figure 97 shows a plot of the measured, normalized air permeability as a function of time, for the array of five boreholes 57 – 61. Note the downward trend of many measurements below the normalized value of one. In particular, the data for borehole sections 59-2 and 59-3, reproduced in Figure 98, exhibit the downward trends prior to December 1999. These data imply that liquid saturation in the fractures in the vicinity of these borehole sections continue to increase until December 1999. The subsequent upward trend of permeability values in these borehole sections signify drying, as a result of the expansion (with time) of drying around the Heated Drift and the wing heaters. These measurements validate the model simulations. Figure 99 shows the simulated fracture liquid saturation for September 1999, December 1999, March 2000 and June 2000. Borehole 59, the third borehole from the top, has the lowest elevation of the three boreholes above the heater plane. Borehole sections 59-2 and 59-3 are respectively the zones bounded by the temperature sensors (white circles) between x of approximately –16 m to – 8 m, and x of approximately –8 m to 1 m. Note how the liquid saturation in these zones progresses from wet (blue shading) to dry (red shading), which is consistent with the air- permeability measurements.

Further, large decreases in air-permeability measurements also coincide with times when large amounts of water can be sampled. For example, in 59-2, 2.6 liters were collected on October 27, 1999; in 59-3, 1 liter was collected on October 27, 1999, and another 2.3 liters were collected on November 30, 1999. This also occurred in borehole 60, the fourth borehole from the top in Figure 99. Because of its proximity to the wing heater, simulations show a large increase in liquid saturation in sections 60-2 and 60-3 within three to six months of heating. This is consistent with large air-permeability reductions and the collection of 2 liters of water from 60-3 in January 1998 and 5.7 liters from 60-2 on June 4, 1998 (heating in the DST was initiated on December 3, 1997).

We also note that in Figure 97, for borehole sections 57-3 and 57-4, the measured normalized air- permeability values are above one during the first two years of heating. These two borehole sections are quite far from the heat source, and our TH numerical model predicts little change in the fracture liquid saturation from its preheat ambient values, Hence, these increases in air-permeability may reflect thermal mechanical processes that result in increased fracture apertures.

Geophysical Measurements

Electrical resistance tomography (ERT), crosshole ground-penetrating radar tomography (GPR), and neutron log data are used to validate the process models in the following manner. Simulated matrix liquid saturation contours at different phases of heating are generated in the appropriate planes of geophysical measurement. Zones of drying and wetting from ERT and GPR tomograms at specific measurement times are compared to

the simulated contours of liquid saturation in the matrix. We emphasize here again that the comparison between moisture-distribution measurements and model results is in nature qualitative; we therefore look for trends rather than matching individual measurements. For example, Figures 100 and 101 show a comparison of simulated matrix liquid saturation to the tomograms from GPR. Note that (from Figure 100) at early time, there is mostly wetting around the wing heaters. By 33 months of heating, both the simulation and the measurement exhibit extensive drying around the Heated Drift and the wing heater.

Since neutron logging data are point measurements, locations of drying with time of heating are compared to the progression of the drying front of the matrix simulated liquid saturation. The thermal test team has made animations to correlate the advancement of the 50% simulated matrix saturation contour with time to the drying in boreholes 64–68 from neutron logging and show that they track each other well.

ERT tomogram images are based on volume averages on a much larger scale and should not be compared to simulated matrix liquid saturation in detail. Therefore, for validation of modeled results to ERT data, we look for corroboration of drying around the heat source and wetting beyond, and their evolution with time.

4.3.4 Summary

We have found favorable comparison between measurements and modeled results. For temperature, the mean error in ~1700 sensors is on the order of a few degrees Centigrade. Model predictions of signatures of TH coupling in temperature can be correlated to the temperature data. For redistribution of moisture, locations of dry-out and wetting from condensation deduced from ERT, GPR, neutron logs and air permeability in general corroborate well with simulated time evolution of the liquid saturation changes in matrix and fractures.

The favorable comparison of the DST TH models with observations for both temperature and moisture redistribution demonstrates that major components of the thermal hydrological processes are included in the TH process models. The objectives of acquiring a more in-depth understanding of the coupled processes and validating the conceptual TH processes at a drift scale are being met in the DST.

4.3.5 References

CRWMS M&O 1998. *Drift Scale Test Progress Report No. 1.* BAB000000-01717-5700-00004 REV.01. Las Vegas, Nevada: CRWMS M&O. ACC: MOL.19990209.0240

Tsang, Y.W., J. Apps, J.T. Birkholzer, J.E. Peterson, E. Sonnenthal, N. Spycher, and K.H. Williams, 1999.Yucca Mountain Drift Scale Test Progress Report, Lawrence Berkeley National Laboratory LBNL-42538, , Berkeley, California.

Table 2 Comparison of modeled and measured temperatures from approximately 1700 resistance temperature devices (RTDs) in 26 boreholes at selected times during the heating phase of the DST.

Time (months since initiation of heating)	*Statistics from numerical model in which wing-heater gridblocks are assigned rock properties as the rest of the test block*		*Statistics from numerical model in which wing-heater gridblocks are assigned fracture permeability several orders higher than the rest of the test block*	
	Mean Error (ME) (°C)	Root Mean Square Error (RMSE) (°C)	Mean Error (ME) (°C)	Root Mean Square Error (RMSE) (°C)
6	0.70	5.87	0.01	5.63
12	2.41	9.15	-0.15	7.21
18	4.24	11.15	0.90	8.72
24	Not available		1.06	9.79
30	Not available		1.27	10.49
33	Not available		1.65	10.61
36	Not available		2.01	11.27
39	Not available		2.77	11.98

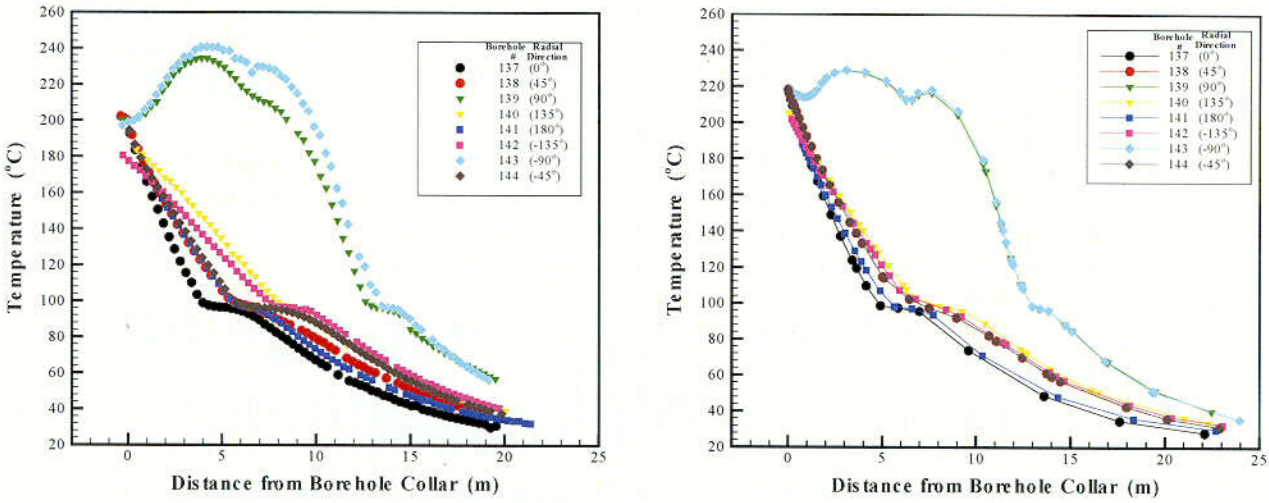

Figure 92 Temperature profiles for boreholes 137 –144 at 33 months of heating, for both measured (left) and model predictions (right).

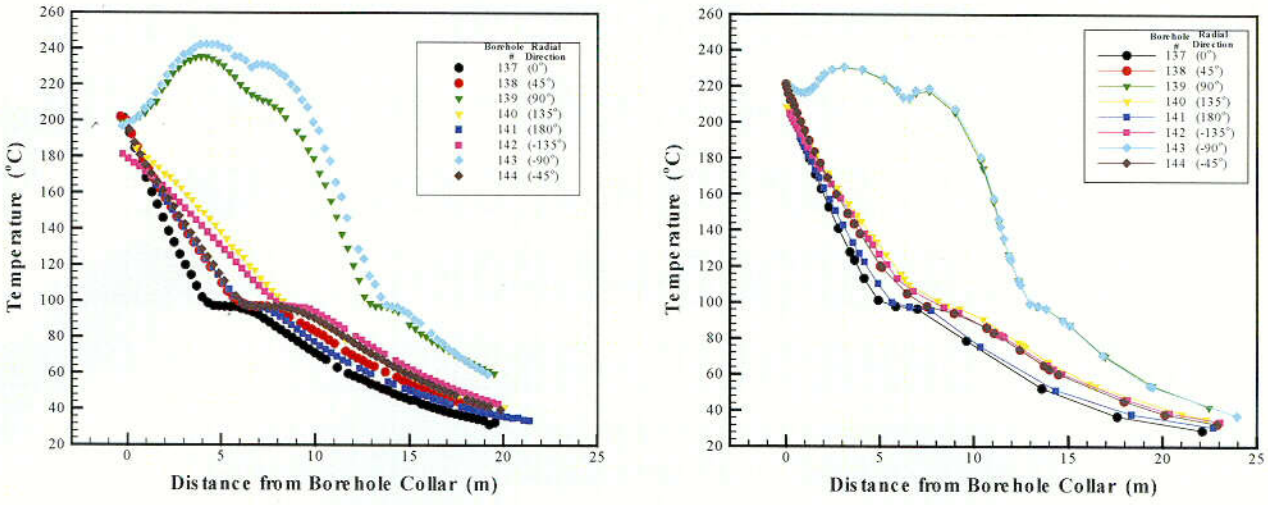

Figure 93. Temperature Profiles for Boreholes 137 –144 at 36 Months of Heating, for Both Measured (left) and Model Predictions (right)

C04

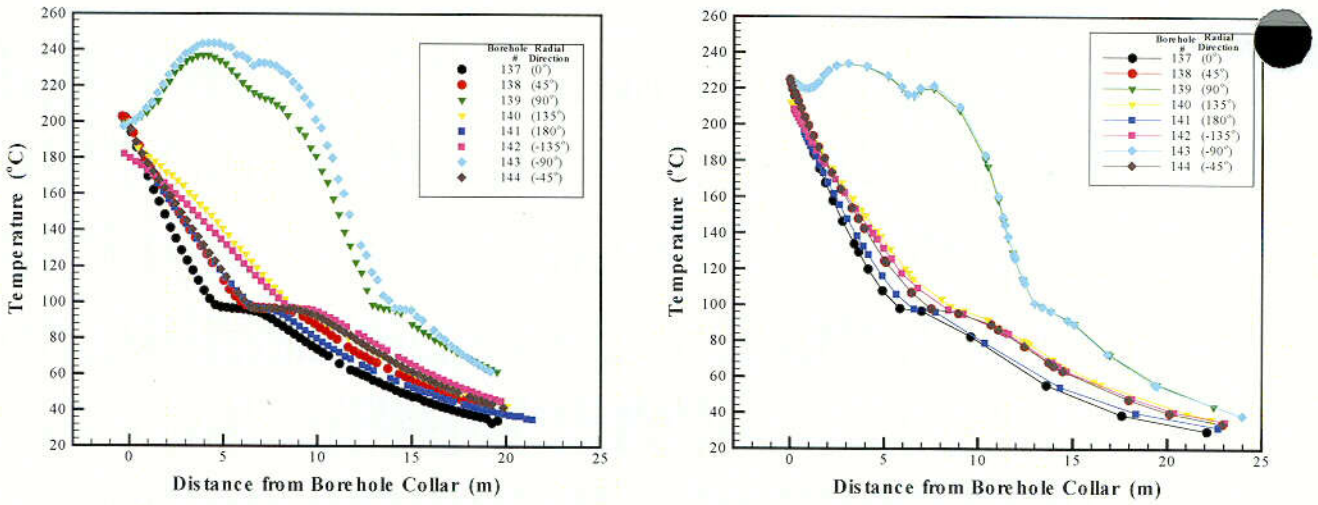

Figure 94. Temperature Profiles for Boreholes 137–144 at 39 Months of Heating, for Both Measured (left) and Model Predictions (right)

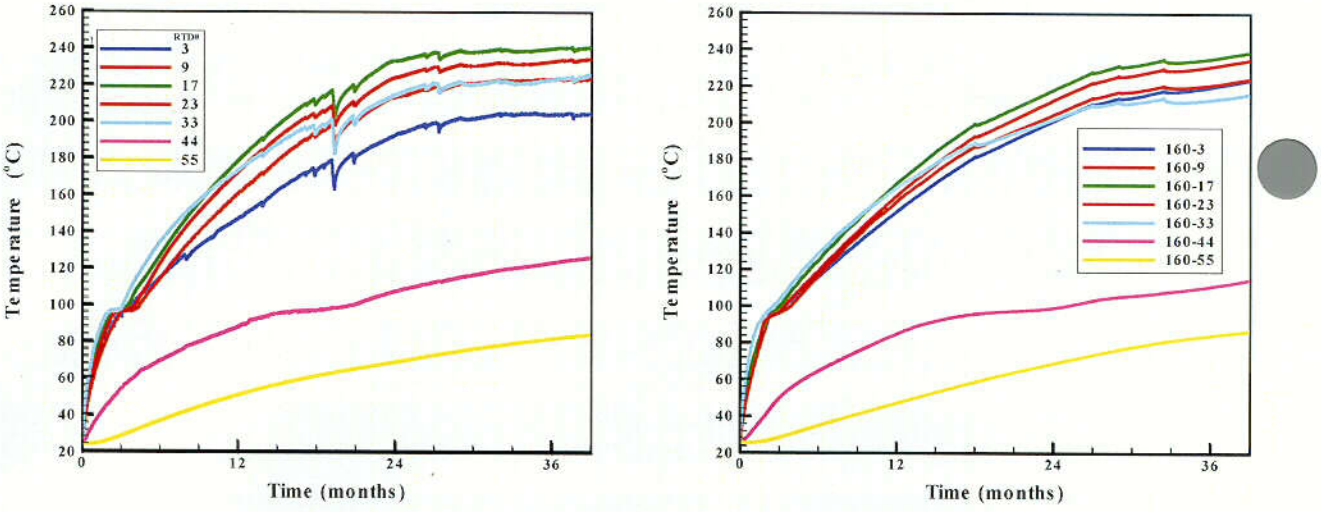

Figure 95. Temperature History of Selected Sensors in Borehole 160, a Horizontal borehole Slightly above the Wing Heaters

C05

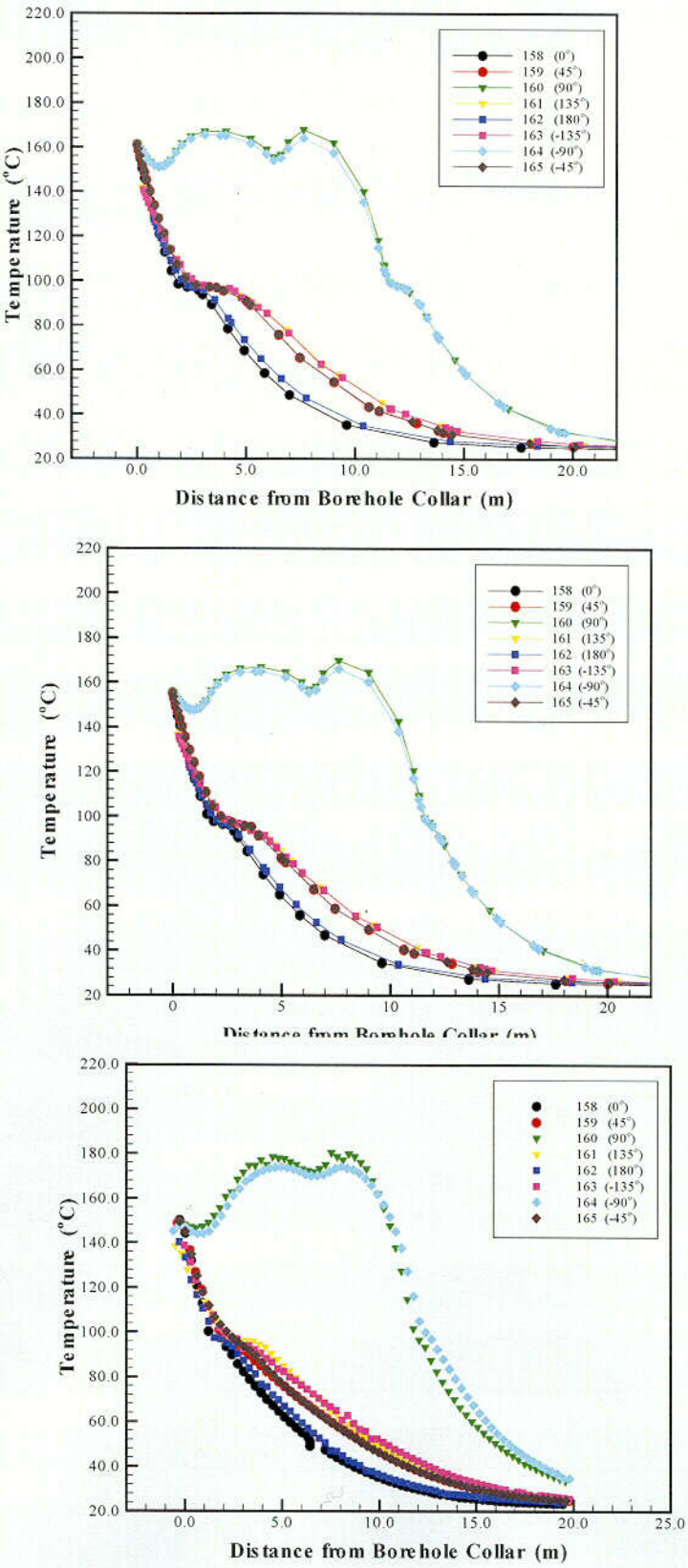

Figure 96. Temperature Contours for Borehole array 158–165 at 12 Months of Heating for Modeled Predictions When (a) Wing Heater Gridblocks Are Assigned Rock Properties, (b) Wing Heater Gridblocks Are Treated as High-Permeability Conduits, and From (c) Measured Data

C06

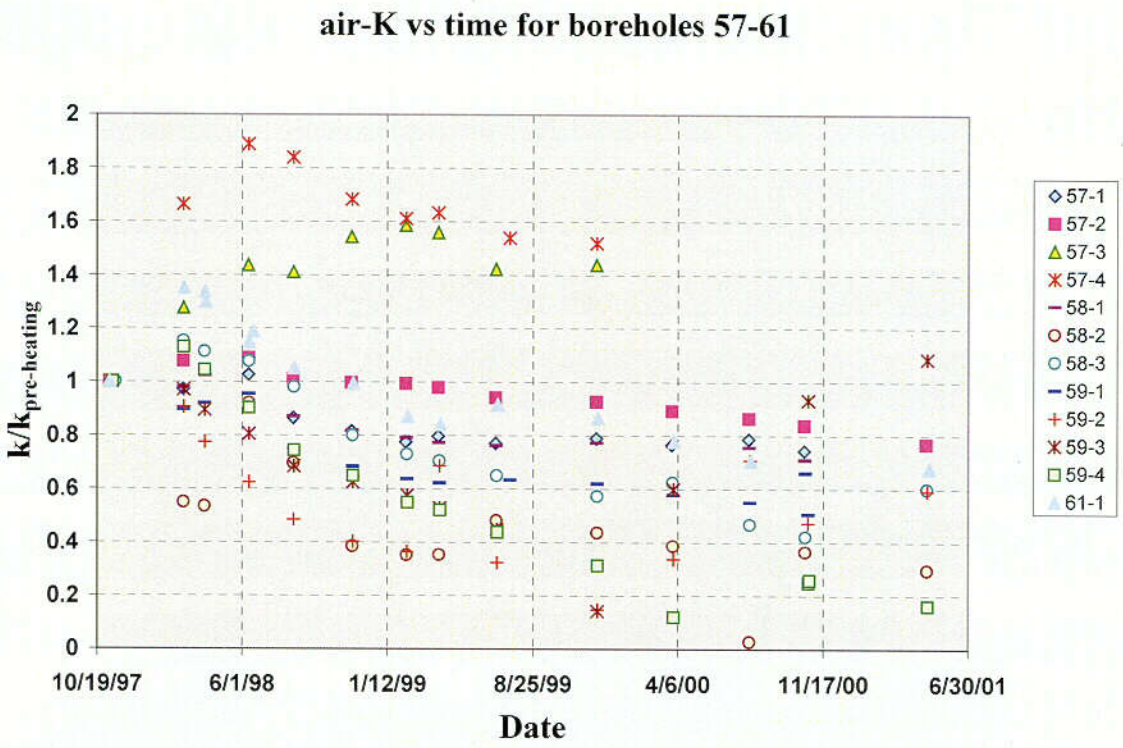

Figure 97. Measured Air Permeability (Normalized to Preheat Values) as a Function of Time for Borehole Array 57–61

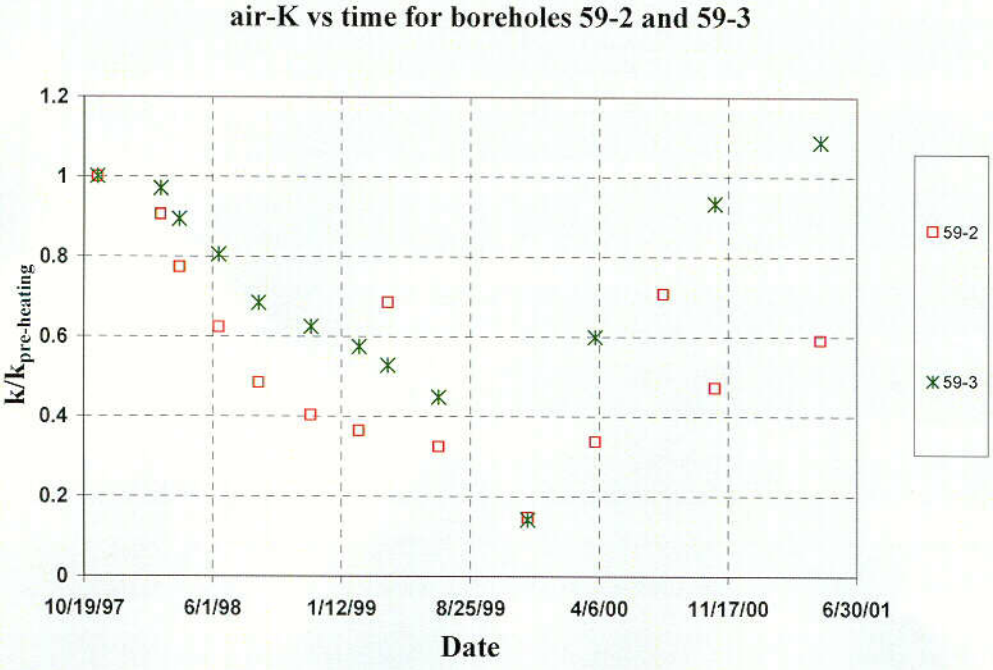

Figure 98. Measured Air Permeability (Normalized to Preheat Values) as a Function of Time for Zones 2 and 3 in Borehole 59

C07

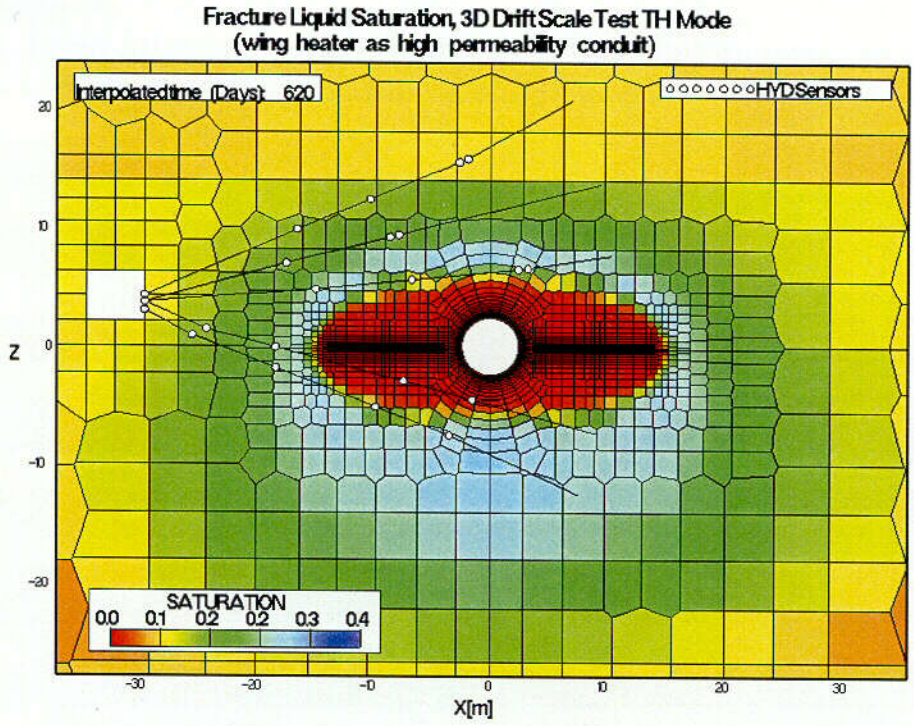

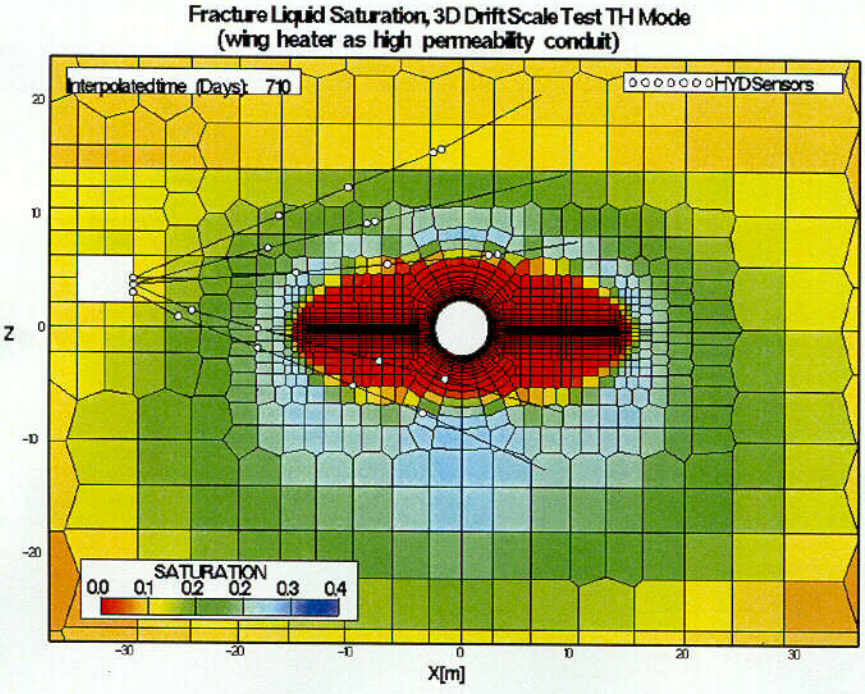

Figure 99. Simulated Liquid Saturation in the Fractures for September 1999, December 1999, March 2000, and June 2000, to Illustrate How the Borehole Sections 59-2 and 59-3 Evolve from Zones of Wetting to Zones of Drying

C08

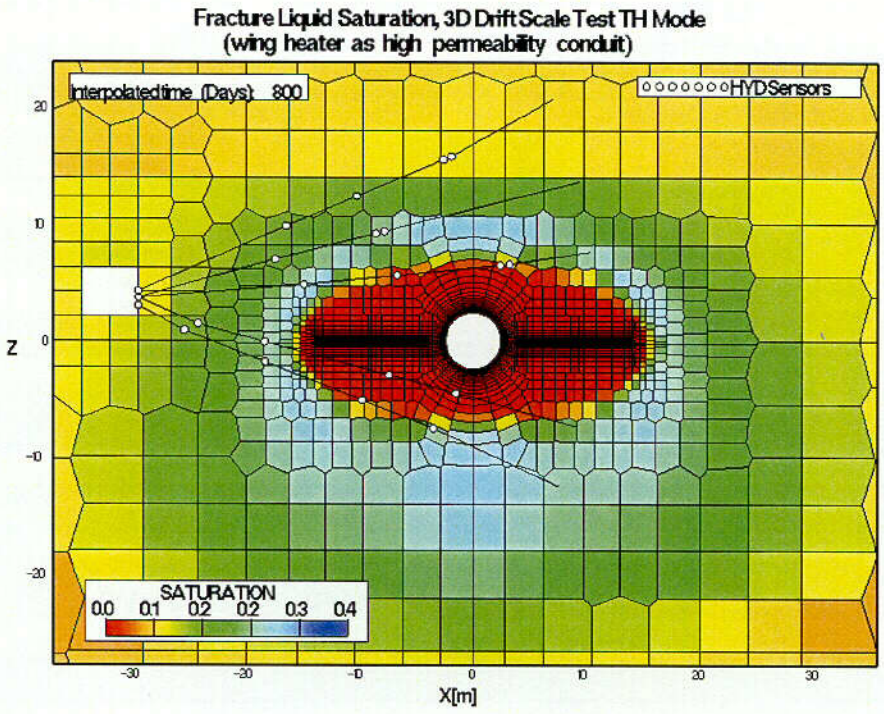

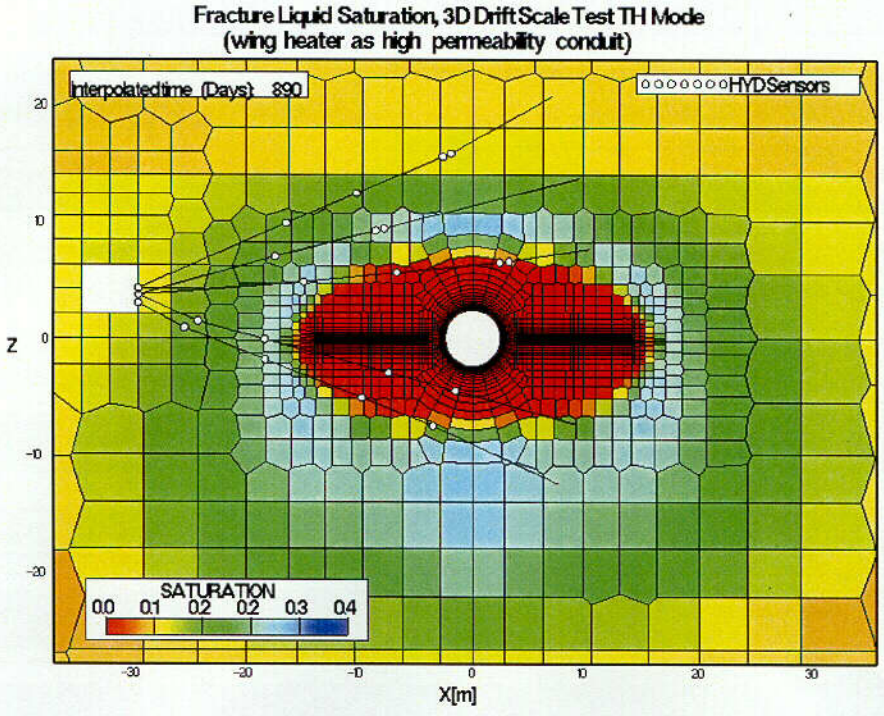

Figure 99 (continued). Simulated Liquid Saturation in the Fractures for September 1999, December 1999, March 2000, and June 2000, to Illustrate How the Borehole Sections 59-2 and 59-3 Evolve from Zones of Wetting to Zones of Drying

C09

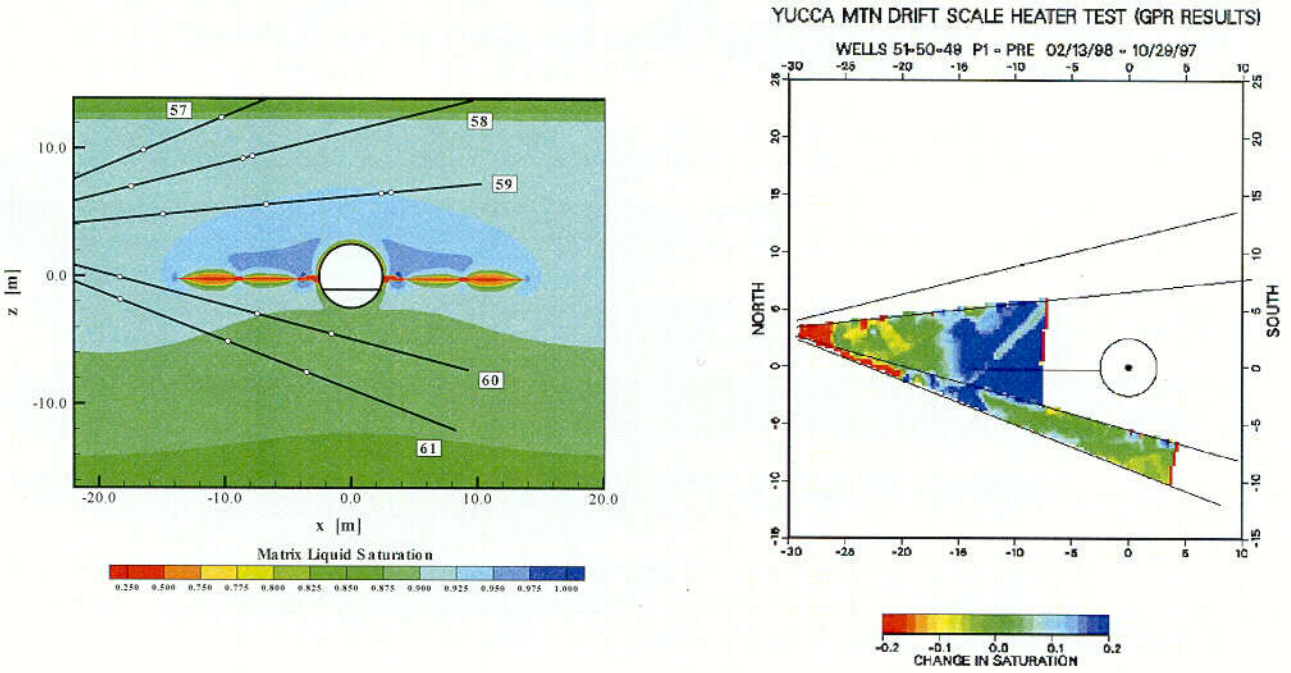

Figure 100. Corroborating the Simulated Liquid Saturation in The Matrix At Three Months of Heating to The Change in Saturation from Preheat Values Deduced from The Tomogram of GPR Measurements Made at ~ 2 1/2 Months of Heating.

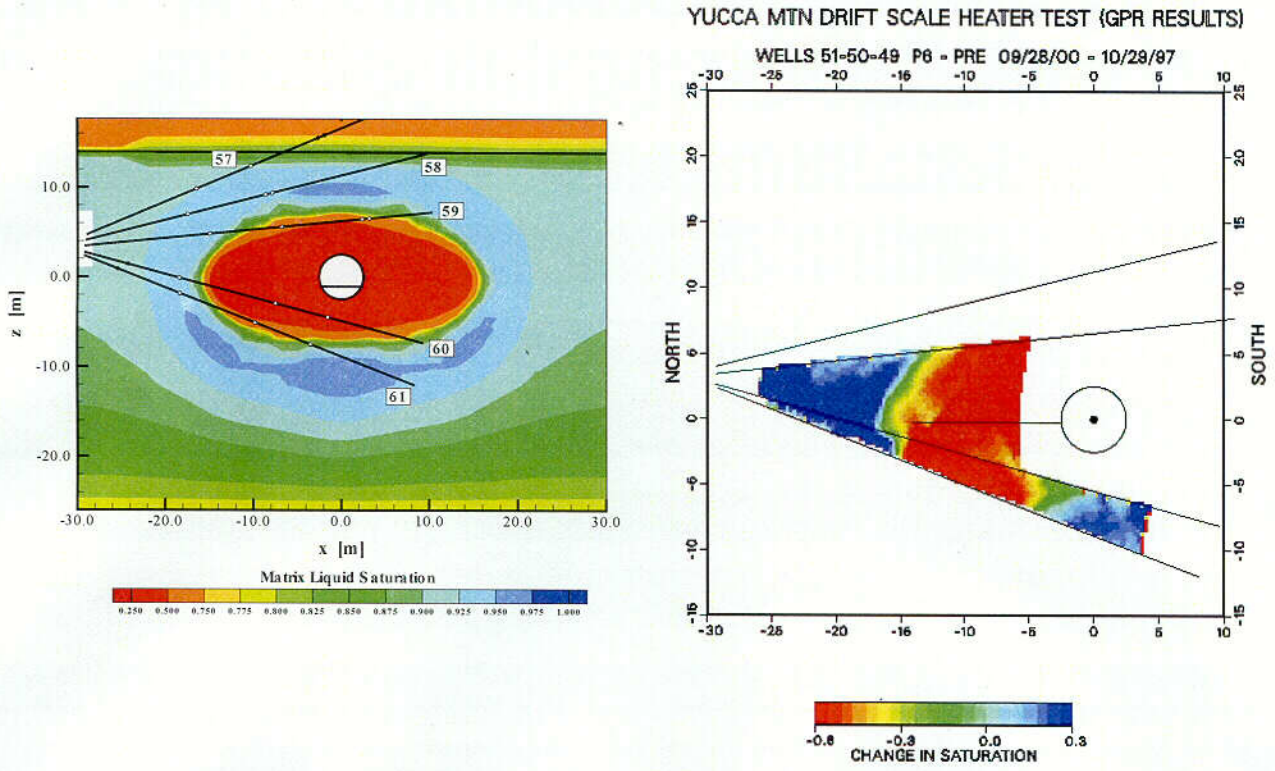

Figure 101. Corroborating the simulated liquid saturation in the matrix to the change in saturation from pre-heat values deduced from the tomogram of GPR measurements, at 33 months of heating.

C10

4.4 Neutron logging and temperature in borehole 79

The purpose of this section is to use the neutron logging caused thermal perturbations in borehole 79 to recognize and understand the thermal and hydrological processes that are occurring within the Drift Scale Test. The discussion will include the construction of the borehole, patterns that are present in the temperature data, and some possible explanations for these patterns and the physical processes occurring. Not all anomalous patterns of borehole 79 are addressed here.

Borehole locations and construction
Boreholes 79 and 80 are parallel to the heated drift as shown in Figure 98, and about 3.5 meters above the wing heaters or about 1 meter above the level of the top of the heated drift. These boreholes are about 9.5 meters to the right and left of the centerline of the heated drift and serve as neutron and temperature measuring boreholes.

Borehole 79 was constructed by drilling and then inserting a Teflon pipe with RTDs fixed to the exterior into the drilled borehole. The RTDs are in two bundles with sensors placed 2 meters apart in each bundle. The RTD bundles are staggered by 1 meter resulting in an RTD each meter. Centralizers were used to nominally place the Teflon pipe near the center of the borehole. Grout was pumped into the annulus between the Teflon and the borehole wall. The RTDs are probably somewhere in the grout, perhaps closer to the Teflon and perhaps closer to the wall rock. It is possible that the Teflon pipe was rotated during the construction process so the RTDs may be near the top of the borehole or nearer the bottom of the borehole. Nothing really sticks to Teflon so it is likely that a very small annulus could exist between the Teflon and grout. This borehole is believed to have a downward slope with the back of the borehole nearly a meter below the collar. The highest numbered RTDs are near the back of the borehole. The borehole was partially blocked at the time of Teflon pipe placement so the deepest RTD is at about y = 42. The wing heaters are located between y = 1.8 meters and y = 45.8 meters. The seven lowest numbered RTDs are actually in the connecting drift and the temperature fluctuations measured reflect seasonal variations in the ESF.

Borehole 80 is constructed similarly with the differences that 1) the borehole was not blocked so RTDs extend all the way to the bottom of the borehole, 2) the borehole is believed to be more horizontal with the bottom of the borehole nearly at the same elevation as the collar, 3) the RTDs are not sequentially numbered.

Figure 102 shows the temperatures measured in borehole 79 against time. Neutron logging events are illustrated as vertical lines. The lowest numbered RTDs are the coolest on the chart. RTDs 1-7, which are all located in the connecting drift, act in unison and show the seasonal variation in ESF temperatures. RTDs 8 and 9 which are located in the borehole relatively short distances show a slightly warmer somewhat damped pattern similar to RTDs 1-7.

Fluid Events: Close examination of the RTDs with temperatures below boiling show smooth and consistent but relatively slow increases in temperature until about day 850. Beginning on about day 850 RTDs numbered 18 through 13 experience, in that order,

relatively rapid and irregular increases in temperature. It seems likely that a different process is at work to create these higher temperatures. It is unlikely that rock/grout temperature got that much hotter that quickly however the introduction of fluid (gas or liquid) could raise the temperatures measured by the RTDs very quickly. About 30 days separate the beginning of the rapid increase in temperature for RTD 18 and RTD 13. These two RTDs are about 5 meters apart. For the remainder of this discussion this type of rapid increase or decrease in temperature which is attributable to the presence of a fluid with a temperature different than the surrounding rock/grout temperature will be referred to as a fluid event.

Neutron logging events: The pattern of the fluid event illustrated in RTDs 13 – 18 beginning at about day 850 is sharply broken on day 894 coincident with a neutron logging event. The temperatures for these RTDs drop nearly to their pre-fluid event temperature. In other words, The neutron logging event stops the effects of the fluid event.

In the process of neutron logging the majority of water is removed from the borehole by swabbing, running a cloth rag into the borehole and pulling it back out. As the swab is removed it may be damp, very wet, or even pushing water out of the borehole in front of the wet cloth. This swabbing process is repeated until the cloth returns no wetter than damp. There is sometimes a pneumatic pressure/vacuum that builds up in this swabbing process.

Fluid and Neutron logging events: Examination of Figure 102 shows a clear pattern of fluid events in which RTDs with temperatures below boiling get hotter and RTDs with temperatures above boiling get cooler and neutron logging events which seem to stop the effects of the fluid events. The neutron logging events appear in Figure 102 as instantaneous events while the fluid events occur at different times in different places. The fluid events do not occur in all RTDs at the same time but rather show the movement in space of the fluid event. The fluid event is probably not the flooding of an area with a vapor of different temperature but rather the initiation of a circulation pattern from a source.

The presence of a long-lived fluid circulation event represents a different mechanism of thermal transfer within the rock/grout.

Fluid and Neutron Logging events in Space: Figure 102 illustrates the timing of the fluid and neutron logging events. It is also important to consider spatial aspects of these phenomenon. Figure 103 is a detailed look at a small area for a relatively short period of time. That short period of time includes a fluid event and a neutron logging event. The X axis present on Figure 103 represents the Y coordinate from Y = -6 to Y = 3. The RTD at Y = 0.5 meters is not functioning. The time period represented is from 840 to 902 days in 4 day increments. 1) The isochrons for 840 through 852 days represent the rock/grout temperature before the introduction of hotter fluid. 2) The time period from 856 to 892 days represent the introduction of hotter fluid. Beginning with the RTD at –0.5 meters the temperature steadily rises affecting RTDs from –0.5 to –5.5 meters. 3) Following the

neutron logging event on day 894 the temperatures are slightly warmer than the beginning temperatures. The temperature for this entire time period at Y = 1.5 meters has remained essentially the same at very near the boiling point. The data gives the feeling that the hotter fluid was entering this snapshot from the right or the positive Y direction.

Figure 104 is a detailed look at the same time period as figure 103, but in the area from Y = 0 to y = 40 meters. This is the portion of the borehole that is located approximately above the heaters and is all above boiling. As in Figure 103, figure 104 includes background conditions, a fluid event, and a neutron logging event. The data at 30 to 40 meters shows very regular behavior through time where there are no crossing lines. This indicates a gradual heating of the rock with no perceived effect of fluid events and no effect of neutron logging.

That portion of the data between about 15 and 30 meters has a somewhat saw-toothed appearance in which every other RTD shows both high and low extremes while the intervening RTDs are more moderate. A look at this section of the plot through time shows the effects of both the fluid event and the neutron logging event. Temperatures in the pre-fluid event time represented by days 840 – 852 in figure 104 show a saw-tooth pattern which suggests that every other sensor is experiencing hotter temperatures than its neighbors. This is likely if the hot RTDs are located nearer the heaters than cool RTDs. Construction information suggest this is possible. The fluid event cools the RTDs beginning near the Y = 10 meter position with the cooling spreading toward right on the diagram eventually cooling as far as about Y = 27 meters. Those RTDs which were hottest and construed to be lower are cooled the most suggesting that fluid path is nearer the lower (hotter) RTDs than the higher (cooler) ones. After the neutron logging event on day 894 the temperatures regain the pattern of before the fluid event but slightly hotter indicating the rock has continued to be heated.

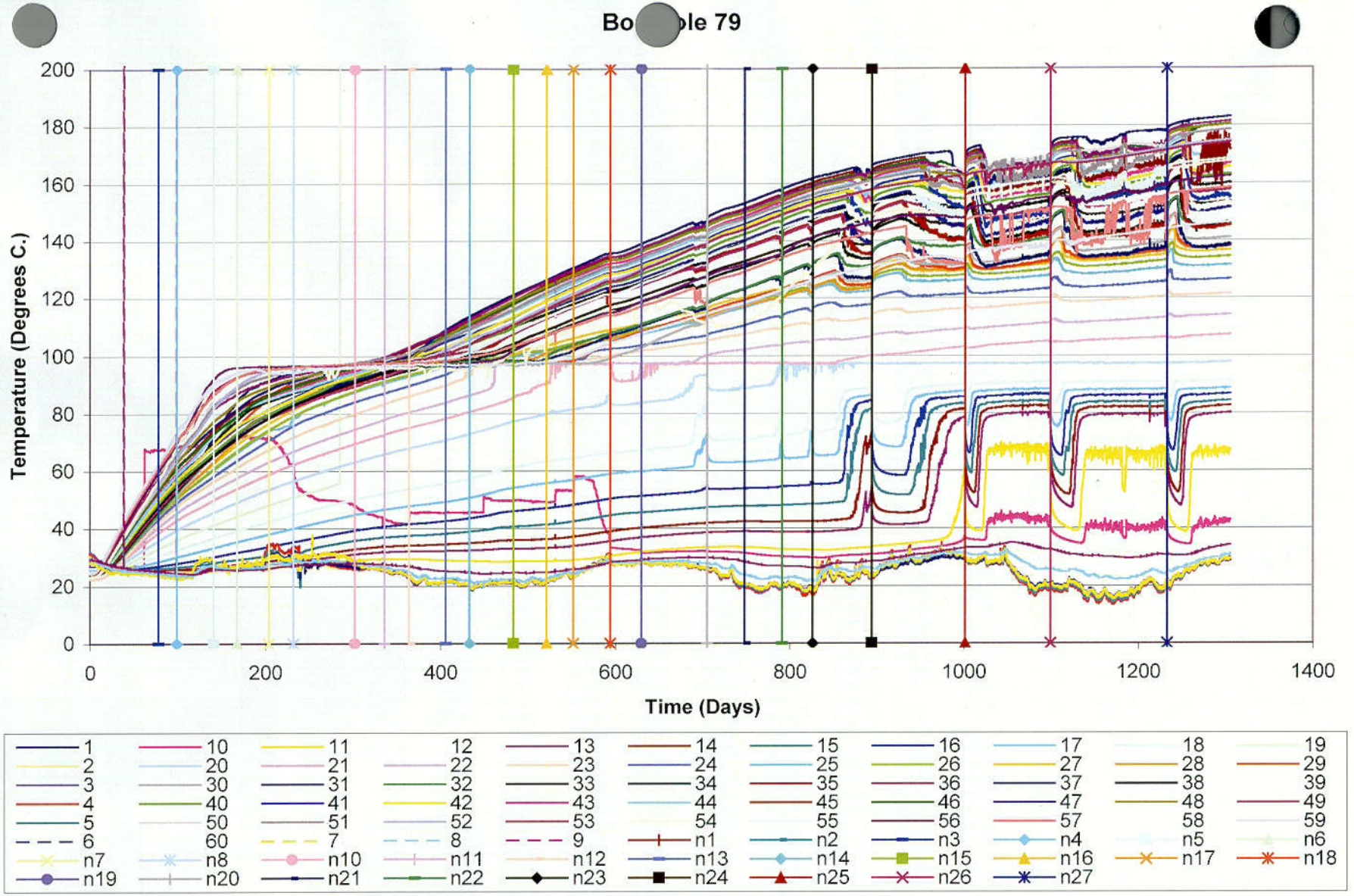

Figure 102. Temperatures and neutron logging events as a function of time for borehole 79.

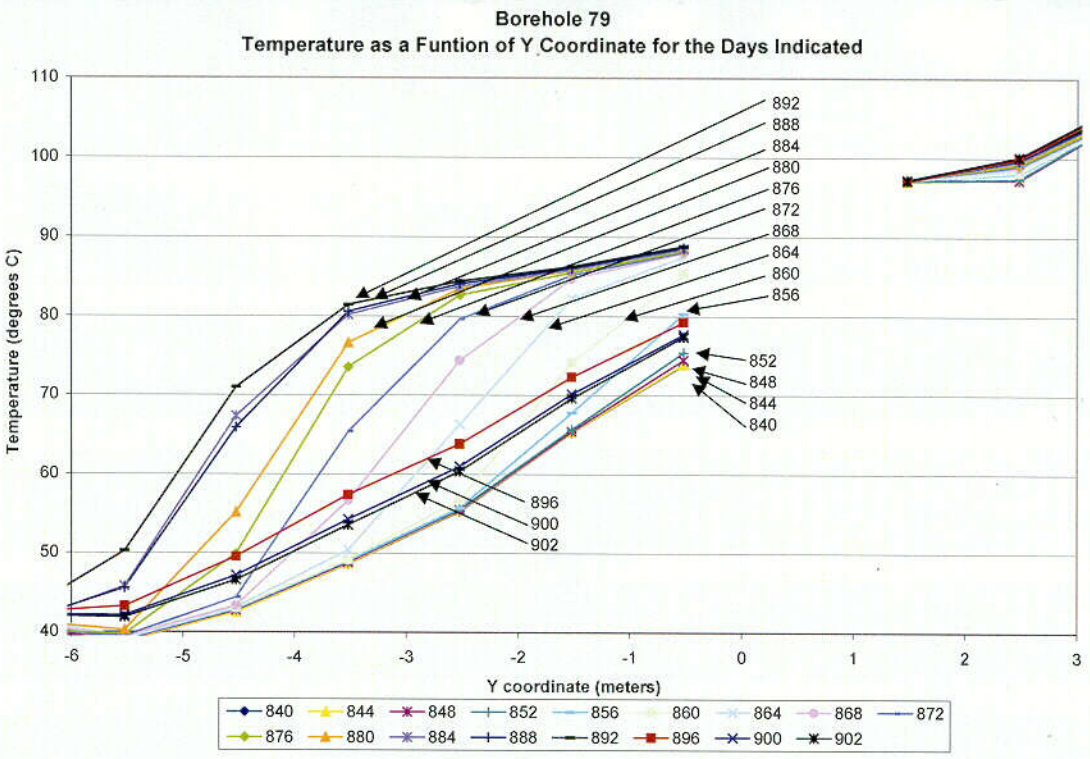

Figure 103. Temperature as a Function of Y Coordinate for Fluid and Neutron logging event.

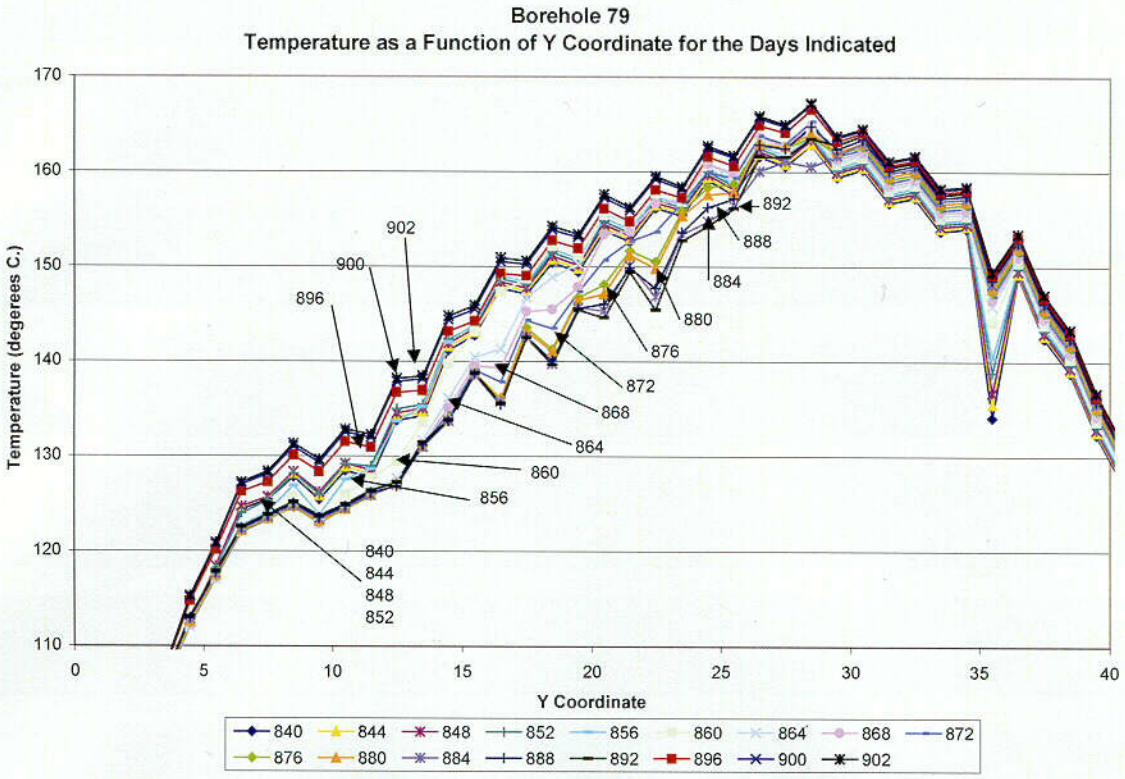

Figure 104. Temperature as a Function of Y Coordinate for Fluid and Neutron Logging Event.

C12

INTENTIONALLY LEFT BLANK

5. Thermal-Mechanical Processes

Thermal-Mechanical process are discussed in four sections in this chapter. Sections 5.1 and 5.2 present thermal mechanical data and deformation and section 5.3 discusses THM model validation. Section 5.4 discusses acoustic emission/microseismic monitoring.

5.1 Thermal-Mechanical Data from the Drift Scale Test, 9/1/2000 – 3/31/2001

This short report discusses the results of strain gage data taken from the concrete liner and unconstrained concrete coupons in the Heated Drift, as part of the Drift Scale Test. The presentation of these data includes updating with recent measurements taken from the Drift Scale Test through 3/31/2001. The discussion here was presented at the 12th Thermal Test Workshop held in Las Vegas, NV, on June 7-8, 2001.

The discussions during this Thermal Test Workshop differed from previous workshops in that the primary themes were related to how the DST data can be used for performance confirmation and performance assessment. The mechanical data discussed during this workshop were the recent Plate Loading Test data, the MPBX displacement data, and acoustic emissions data. These data are used for design and performance assessment purposes in the following manner.

Design Issues
- Rock mass mechanical properties (elastic modulus, thermal conductivity) important to the design of a facility
- Development of new fractures (acoustic emissions, changes in MPBX data) that may indicate structural integrity issues

Performance Assessment (Coupled THM)
- Evidence of fracture deformation, either in the formation of new fractures, or in changes to existing fractures (shear slippage, aperture changes)
- Resulting changes in permeability which may affect water/vapor influx to the drift during cooling

5.1.1 Plate Loading Test performed Oct. 2000

The Plate Loading Tests (PLT) was conducted as part of the Drift Scale Test (DST). The purpose of the PLT was to obtain rock mass elastic modulus measurements under ambient and hot conditions for the middle nonlithophysal tuff. Two earlier tests were conducted in 1998, after which design changes were made to ensure a stiffer loading frame for improved measurements.

The PLT Niche is located about 5 m from the Heated Drift (HD) bulkhead and is driven approximately 5 m toward the north, perpendicular to the axis of the HD. The niche is a roughly 2.5 m diameter alcove with a nominally flat floor. The niche was mined using drill and blast techniques during the construction phase of the DST during early FY98. The PLT is designed to mechanically load the rock in a horizontal orientation using large square-shaped flatjacks that press against both ribs of the PLT Niche. Design of the PLT

reaction frame was predicated on materials having compressive strengths in excess of 55.2 MPa (8000 psi: maximum jack pressure design) and having a minimum Modulus of Elasticity (E) of 30 GPa (4.3512 x 10^6 psi). In addition, the excavated rock surfaces of the PLT niche were required to be prepared in accordance with ASTM D4394-84. The primary design change from the 1998 tests was the use of aluminum rather than stainless steel plates for the load bearing plates. Aluminum allowed for easier installation of the plates, resulting in very little need for pre-test shims to eliminate unwanted gaps in the plates. This stiffer frame design produced negligible displacement of the plates during pressurization, thus directing all the displacing force from the flatjacks into the surrounding rock mass. The PLT setup is shown below in Figure 105.

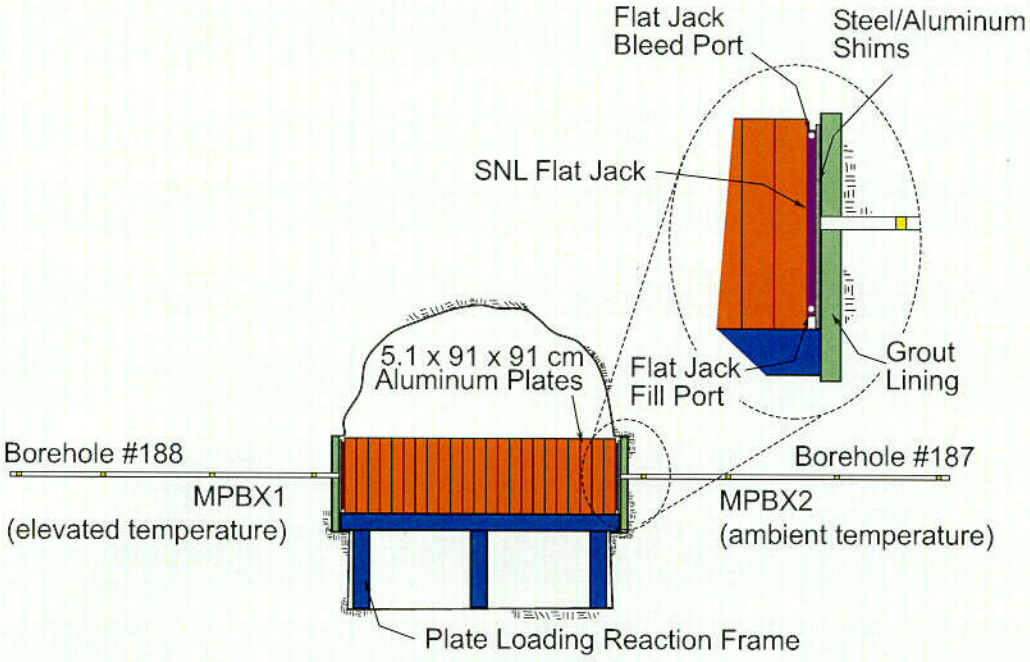

Figure 105. Plate Loading Test Setup

The displacement measured at the deep anchor, ambient side in response to the pressurized flatjacks is shown in Figure 106. The pressure was increased in a stepwise fashion, with intervening periods where the pressure was reduced. This cycling of the pressure in the flatjacks can be seen in the hysteretic behavior of the rock, which relaxes at a different modulus than when it is compressed. The rock was eventually pressurized to a maximum bearing pressure ~32 MPa (4600 psi), resulting from a maximum flatjack pressure of about 6000 psi. The temperatures in the hot and ambient sides of the test were T_{hot} = 58°C, $T_{ambient}$ = 36°C.

The resulting values of rock mass modulus from the October 2000 test, as well as from the 1998 tests, are shown in Table 3. The recent test measured higher rock mass elastic modulus values than did the 1998 tests. Some of this difference is due to the improved testing technique. There is expected to be one more plate loading test in the fall of 2001 before the heat to the DST is shut off in January 2002.

C13

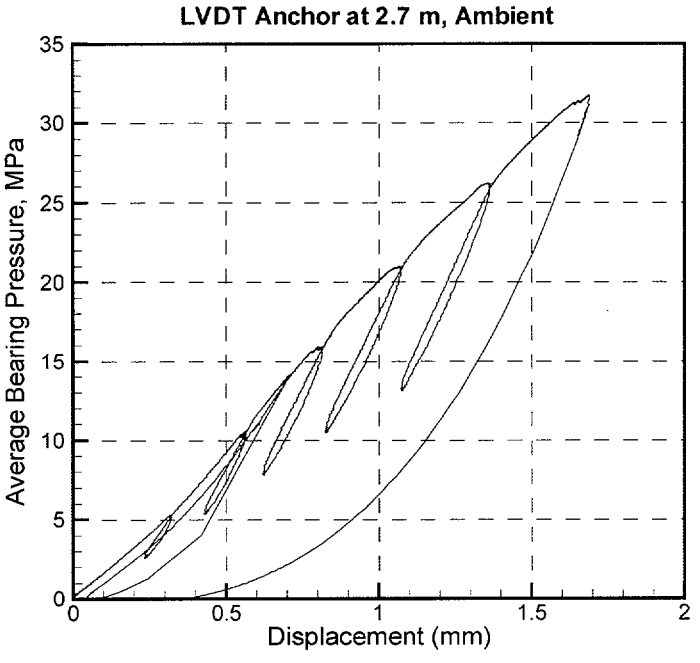

Figure 106. Measured Displacement of the Deep Anchor, Ambient Side During the PLT

Table 3. Calculated Elastic Moduli from the Plate Loading Tests

Plate Loading Test Date	Maximum Bearing Pressure (MPa)	Ambient side of PLT Niche (GPa)	Heated side of PLT Niche (GPa)
5/28/1998	6.4	**Deep – 11.7** Middle – 12.3 Shallow – 14.6	Deep – 30.1 * **Middle – 26.6** Shallow – 33.8
6/9/1998	11.9	**Deep – 11.4** Middle – 12.9 Shallow – 16.2	Deep – 29.7 * **Middle – 30.2** Shallow – 37.6
10/17/2000	31.75	**Deep – 17.3** Middle – 19.6 Shallow – 24.2	Deep – N/A **Middle – 43.0** Shallow – 53.2

* - The hot side, deep anchor results are questionable due to problems with that LVDT.
The results in **bold print** are the recommended modulus values from each test.

5.1.2 MPBX displacement data

For design purposes, the middle nonlithophysal tuff has exhibited behavior that is approximately elastic. Figure 107 compares pre-test predictions of displacement for MPBX-3 with the actual data. The pre-test elastic model using intact rock properties gives reasonably good estimates of rock mass displacement behavior. Note that the displacements for the four anchors increases gradually with time, in a manner similar to the predictions (with the notable exception of behavior with Anchor 4 around 1060 days, which is discussed later).

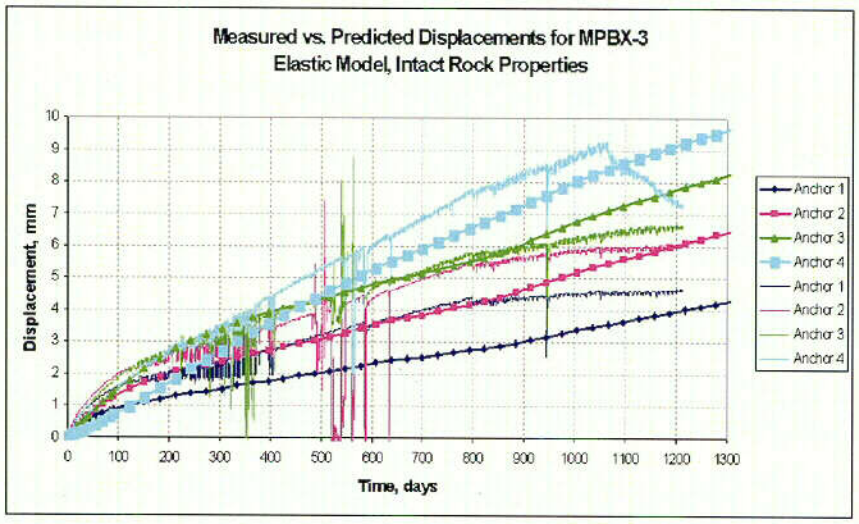

Figure 107. Measured vs. Predicted Displacements for MPBX-3

To date, the MPBX data have shown that the rock expands in a manner consistent with thermoelastic behavior, with a steadily increasing displacement between the anchors and the collar. This increase in displacement is produced by the heated rock expanding into the drift, while the cooler rock further away remains relatively unchanged. As the thermal pulse expands away from the drift, these displacements continue to increase. As the thermal test team analyzes the MPBX data, they search for "events" that may indicate fracture changes. Such changes may later be linked to structural issues for the designers, or to changes in the bulk permeability of the rock which would have consequences for the coupled thermo-hydrologic processes. One such significant event occurs for MPBX-3, in borehole 147. The displacements and temperatures for MPBX-3 are plotted in Figure 108. Anchor 4 of MPBX 3 (15 m from the collar) has a sudden change to its displacement curve beginning on day 1064 (11/1/2000), beginning a steady descent, but the other 3 anchors below it do not display any similar behavior. Because the other three anchors do not exhibit this change, there is no reason to conclude that this is an indication of rock failure near the collar. Additionally, there is nothing in the temperature data at the same time indicating a sudden change in the conditions in this borehole, although the temperature at Anchor 4 (TC-8) does begin moisture-induced oscillations about 100 days before this event. The current hypothesis regarding this event at Anchor 4 is that a major fracture between Anchors 3 and 4 is now sufficiently within the thermal pulse that it is closing. This hypothesis will be investigated further.

Observed deviations from the elastic pattern previously described might signify "events" that could indicate the creation of a fracture, or sudden slippage along an existing fracture. A sudden decrease or increase in displacement in the MPBX data is a potential marker for such an event. Thus, the MPBX data can be used to determine if scaling observed in the Heated Drift thus far is significant. During a recent cleaning and re-

C14

installation of the DST bulkhead windows (April 23, 2001), loose rock was observed at several locations above the welded wire fabric attached to the roof of the Heated Drift. Cables from two instrumented boreholes located 2.7m and 11.9m from the bulkhead along the longitudinal axis of the Heated Drift were observed to have pulled loose from the welded wire fabric. These cables were originally fastened to the wire fabric during installation and remained fastened during prior video imaging in October 2000. This suggests that much of the scaling had occurred since then. This scaling is described in greater detail elsewhere in this progress report. However, one event in the MPBX data that has possible ties to scaling is shown in the data from MPBX-7 (21 m from the bulkhead - see Figure 109). Note that Anchor 1 of MPBX-7 (1m from the collar) begins a abrupt drop in displacement of about 2 mm beginning about day 985 (August 14, 2000). One possible explanation of this drop is a slight loosening of the rock around Anchor 1. However, there is not enough evidence to state this for certain. Anchors 3 and 4 do not show a similar sudden change at this time (Note: Anchor 2 failed earlier in the test). This would indicate that the collar was unaffected by any possible rock movement suggesting the volume of rock affected by fracturing is relatively small. Indeed, the other four MPBXs (MPBX-4, MPBX-5, MPBX-8, and MPBX-9) in the roof at these two stations (13.7 m and 21.0 m from the bulkhead) do not display this behavior. Based on this, it can be concluded that the scaling observed to date is probably due to free surface effects. Therefore this appears to involve only a relatively small volume of rock and not to involve large-scale failure of rock in the roof.

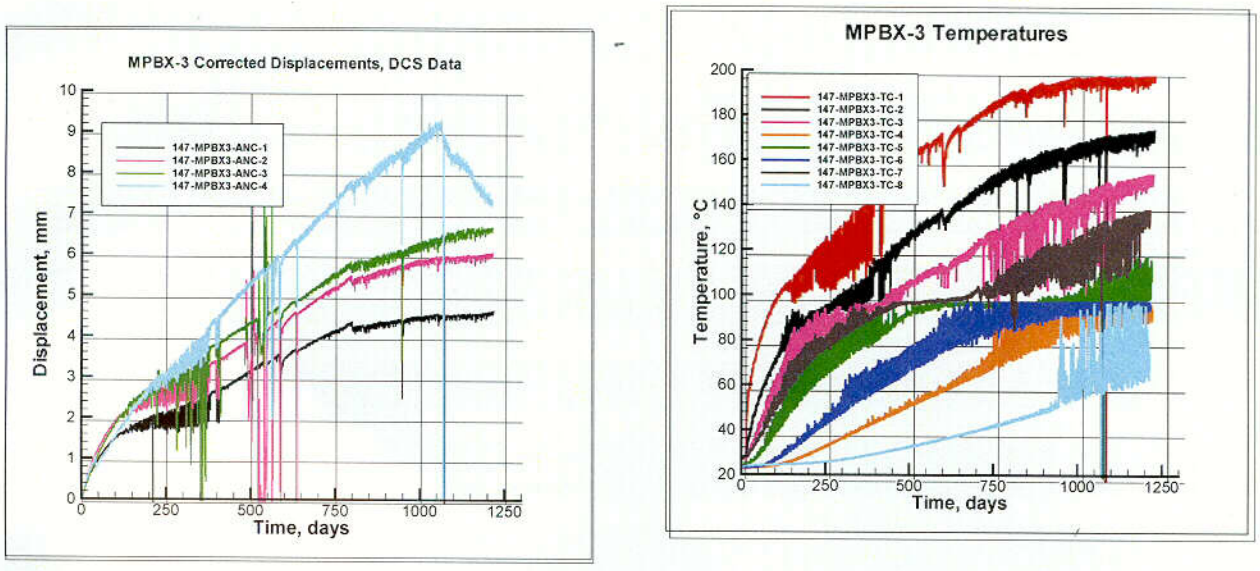

Figure 108. Displacements and Temperatures for MPBX-3 (Borehole 147)

C15

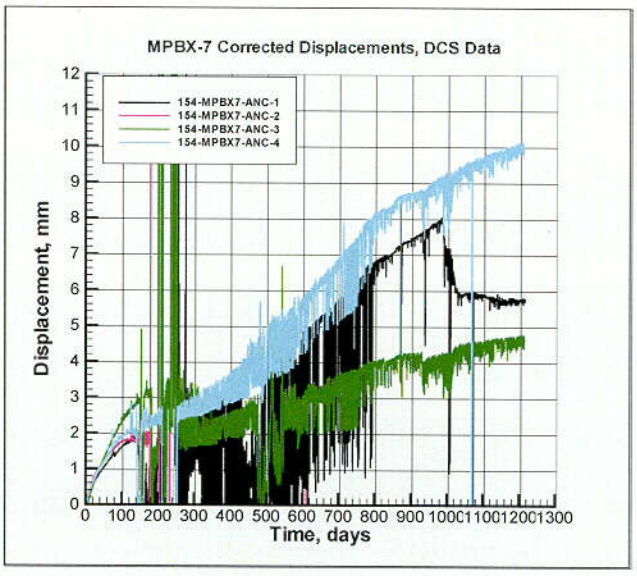

Figure 109. Measured Displacements in MPBX-7 (Borehole 154)

5.1.3 Smoothing effects of moisture-induced oscillations

The MPBX data are meant to provide a measure of rock deformation due to thermal expansion and mechanical stresses in the rock surrounding the Heated Drift. The data were expected to have a "smooth" appearance, with any discontinuities likely relating to sudden movements along fractures. However, many of the data traces exhibit "noise", which makes the data difficult to read and interpret. In general, there are two types of noise that have been identified in the MPBX data. One type is identified by either a wildly oscillating mean value with no discernable pattern, or by values that go outside the expected range of displacement values. These data values are understood to be "bad data", where the gage is experiencing either temporary or permanent incorrect readings. The second type is identified by data that has a discernable pattern (typically, the pattern would follow a curve fit to the top "edge" of the data on a displacement-vs.-time curve), and the data oscillates at values below the predominant curve. These data are being affected by temperature oscillations in the MPBX borehole caused by water recirculation within the borehole. The recirculating water, which alternately boils, rises, condenses, and falls in a cyclic fashion in the borehole, causes the Invar connecting rods to shrink/expand, and also affects the calibration constants of the LVDTs based on the temperature at the collar. It is thought that the surrounding rock mass is negligibly affected by these temperature oscillations, and thus the oscillating MPBX measurements do not represent the actual rock behavior. In order to use the MPBX data to validate thermal-mechanical models, or to use them to derive rock mass thermal-mechanical properties, the true rock mass behavior must somehow be extracted from the noisy data. It is this requirement that led to this initial attempt to smooth the MPBX data.

There are several issues which make a scientifically based algorithm for smoothing the MPBX data a complex matter: the contraction/expansion of the Invar rods, the effect of temperature on the LVDT, the need to capture true fracture deformation events, other causes of unlikely data values. Therefore, as an initial attempt to provide smooth data for

C16

use in validating thermal-mechanical models, a simplified approach using technical judgment was used. Jay Cho (M&O) developed the approach used for this TDIF; after Jay left the YMP, Steve Sobolik (SNL) took on the responsibility of completing this initial data submittal. Under Jay's approach, the acquired MPBX measurements from the LVDTs, as calculated by the Data Collection System, were corrected for the thermal expansion of the Invar connecting rods in essentially the same manner as the developed MPBX data that is regularly submitted to the TDMS. The acquired MPBX and temperature data, and the corrected MPBX data, are listed in an Excel spreadsheet, one for each MPBX. Then, several steps were taken to smooth the data. First, based on the technical judgment of the analyst, sections of data that were considered unusable were deleted from the file. Typically, these data were either the results of a problem with the gage itself: failure, erratic voltage readings, etc. Then, other sections of noisy data were identified using a 0.3-mm difference between values at six-hour intervals. If the behavior of the identified data matched the assumed behavior caused by the recirculating water, then that range of values was discarded. While discarding data, it was important to retain information that may represent other physical processes, such as a sudden permanent shift which may indicate fracture slippage or closure. An example of the results of this smoothing procedure is shown in Figure 110, comparing the before and after plots for data from MPBX-11 (Borehole 178).

This procedure for smoothing the MPBX data can (and likely will) be improved upon in the future. This initial attempt was done to provide smoothed data for use in comparison to the thermal-mechanical analyses in the recently submitted THM-AMR. The data files submitted for this TDIF include data through 7/31/2000 (i.e., through 971 days of heating). For the purposes of the THM-AMR, this is acceptable; at a later date, the project may decide to update all the MPBX data with a more refined smoothing technique.

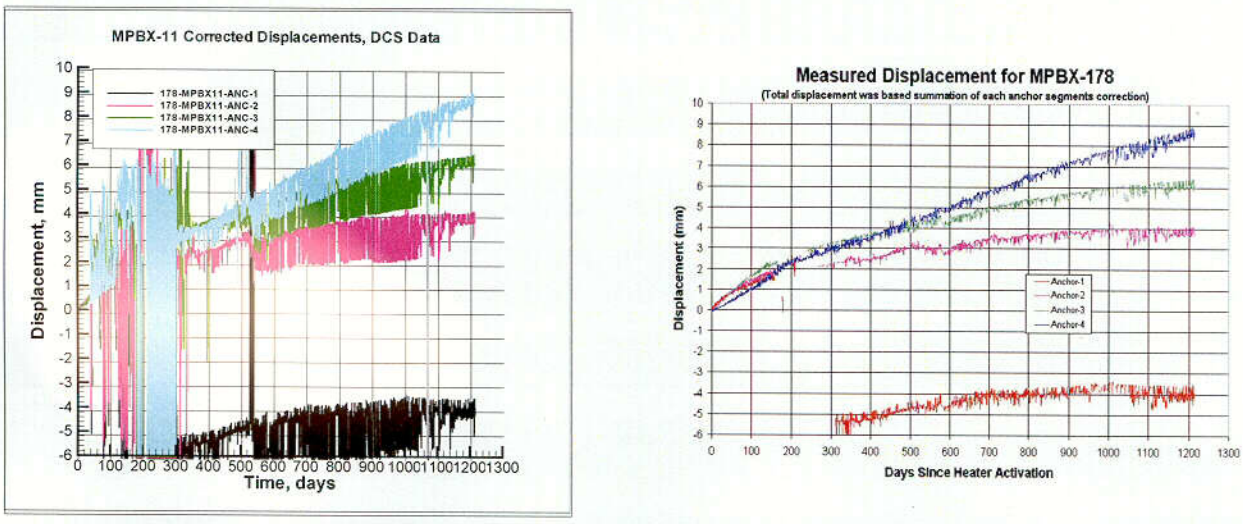

Figure 110. Pre- and Post-Smoothing Plots of Displacement Data for MPBX-11

C17

5.1.4 Comparison of MPBX and Acoustic Emissions Data

Acoustic emissions (AE) data obtained by Lawrence Berkeley National Laboratories are used to determine the occurrence and location of microseismic events caused by the thermal response of the host rock. An earlier comparison of the measurements of the two instrumentation systems (AE and MPBX) identified events monitored by the AE and MPBXs in an attempt to correlate temporally and spatially, and to determine if such correlations are indicative of a rock mass event recorded by both systems. Because of the types of measurements (seismic versus displacement), the frequency of recorded measurements, and locations of the measuring devices, it was unknown whether events such as fracture generation, slippage along fractures, or seismic events would be detected and recorded by both instruments. That earlier study, which examined data through 3/21/2000, found no apparent correlation between MPBX and AE events. With the recent scaling events, more recent AE data were evaluated to determine if any correlations exist between these events. The following conclusions were drawn from this latest comparison:

- There is no apparent temporal correlation between AE data and rockfall events.
- AE data indicates several significant "pops" in the drift crown at earlier times, which may or may not indicate the stress relief that caused the rockfall.
- Rock spalling itself probably does not generate enough signal to register in AE data; the signal is weak, and the high temperatures around it wash that out.

The MPBX and AE data will be looked at on a regular basis to detect any other possible events that might be related to rockfall. This evaluation will take on a greater importance after heater shutdown, when temperatures cool and stresses are relieved.

5.2 Deformation of the Rock Mass as measured by the MPBX

Strain (deformation) was calculated from the displacement data measured in the MPBX boreholes in the DST, so that the responses of the rock mass to the heating are free from the influence of the measurement length. The strain data indicate that most of the deformation is limited to a region within a few meters from the collar of each borehole. The strain data show that the deformation in the region above the heaters is greater than that below the heaters, and that the deformation in the region from-AOD is greater than that in the to-AOD region. These are illustrated by the following figures.

The strain measured in the vertical boreholes are shown in Figures 111 to 116. Figures 111 and 112 show the strain in boreholes #149 and #150 respectively. These boreholes are at 13.7 m from the bulkhead; #149 is vertically up, while #150 is vertically down. The strains between anchors 1 and 2 and the collar in borehole #149 are not available for comparing with that in borehole #150. These two figures are not very good for comparing the strain between the region above the heaters and the region below the heaters. But the strain of anchor 3-0 (the strain in the region between anchor 3 and the collar) in borehole #149 (Figure 111) is greater than that in borehole #159 (Figure 112). Figures 113 and 114 show the strain in boreholes #156 and #157 respectively. These boreholes are at 21 m from the bulkhead. Borehole #156 is vertically up, while borehole #157 is vertically down. Figures 113 and 114 show that the strains in borehole #156 are greater than that in borehole #157. Figures 115 and 116 show the strains in boreholes #180 and #181. These boreholes are at 41.1 m from the bulkhead. Borehole #180 is vertically up, while borehole #181 is vertically down. Figures 115 and 116 show that the strain in borehole #181 is greater than that in borehole #180, opposite to that at 21 m from the bulkhead. But it was reported (Steve Blair, 2001, personal communication) that the displacement measurements in borehole #181 are not reliable due to malfunctioning of the MPBX. In addition, boreholes #180 and #181 are within the section of the HD where the drift is lined with a concrete liner. In summary, the MPBX measurements seem to show that the rock mass above the heater horizon deforms more than that below the heaters.

The deformation of the rock mass in the region toward the AOD (To AOD) and in the region away from the AOD (From AOD) are shown in Figures 117 to 122. Figures 117 and 118 show the strains in boreholes #147 and #148 respectively. These boreholes are at 13.7 m from the bulkhead; borehole #147 is 60 degree away from the AOD, while #148 is 60 degree toward the AOD. Figures 117 and 118 show that the strains in borehole #147 are greater than that in borehole #148. The strains in boreholes #154 and #155 are shown in Figures 119 and 120 respectively. Boreholes #154 and #155 are at 21 m from the bulkhead; #154 is 60 degree away from the AOD, while #155 is 60 degree toward the AOD. Figures 119 and 120 show that the strains in borehole #154 are greater than that in borehole #155. Figures 121 and 122 show the strains in boreholes #178 and #179 respectively. Boreholes #178 and #179 are at 41.1 m from the bulkhead; #178 is 60 degree away from the AOD, while #179 is 60 degree toward the AOD. Figures 121 and 122 show that the strains in borehole #178 are greater than that in borehole #179. In summary, the displacement measurements in the MPBX boreholes show that the rock mass in the region away from the AOD deforms more than that in the region toward the

AOD. This characteristic of the rock mass deformation agrees with the model predictions discussed in Section 5.3.

Figure 111. The strain between anchors #3 and #4 and the collar in borehole #149, which is at 13.7 m from the bulkhead, vertically up.

C18

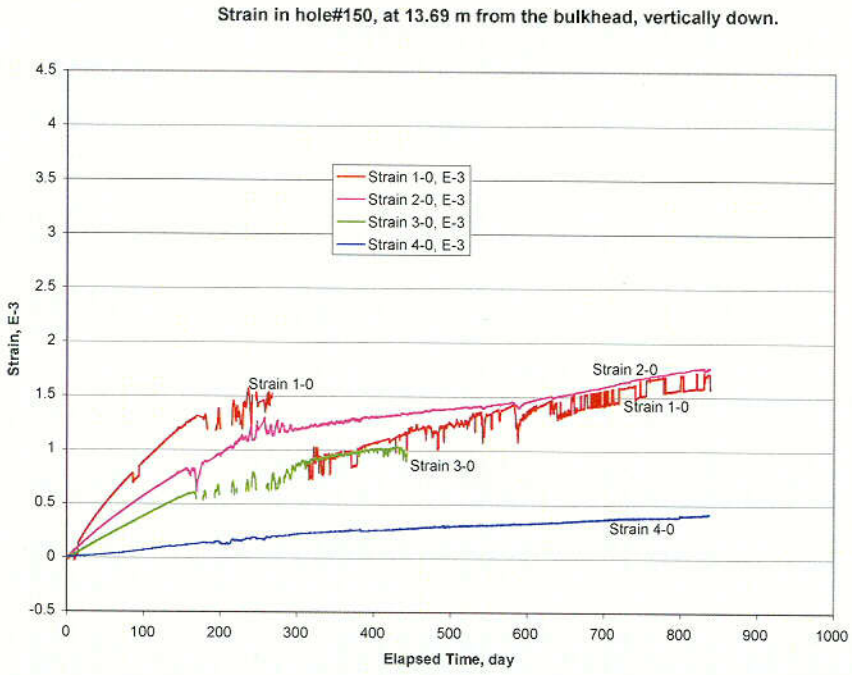

Figure 112. The strain in borehole #150, which is at 13.7 m from the bulkhead, vertically down.

C19

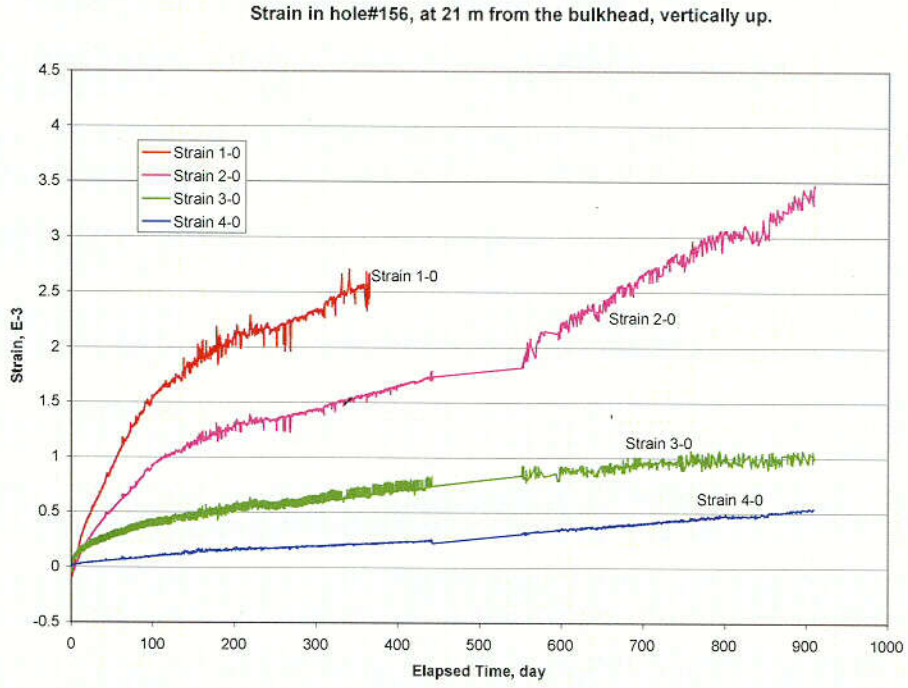

Figure 113. The strain in borehole #156, which is at 21 m from the bulkhead, vertically up.

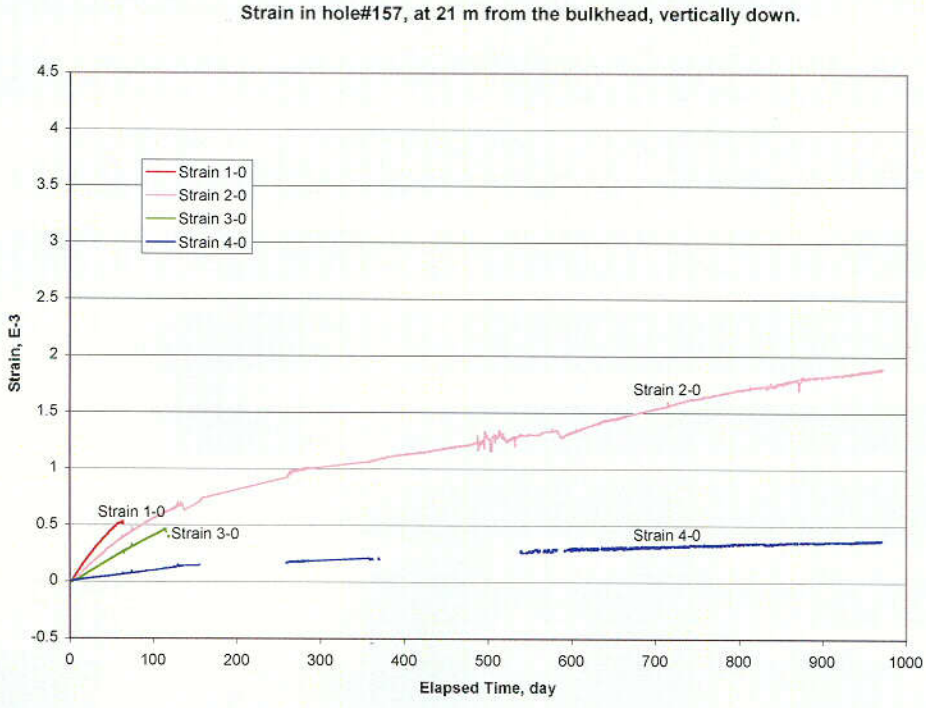

Figure 114. The strain in borehole #157, which is at 21 m from the bulkhead, vertically down.

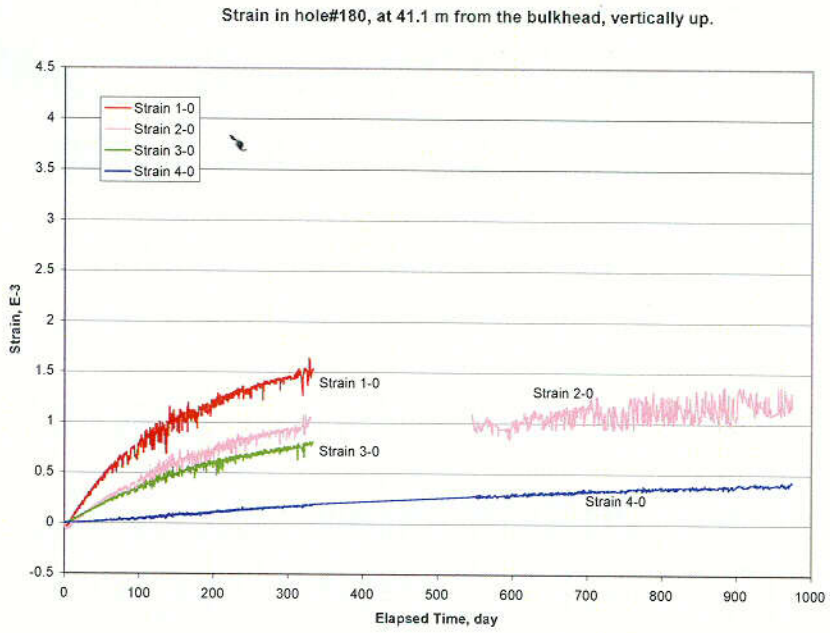

Figure 115. The strain in borehole #180, which is at 41.1 m from the bulkhead, vertically up.

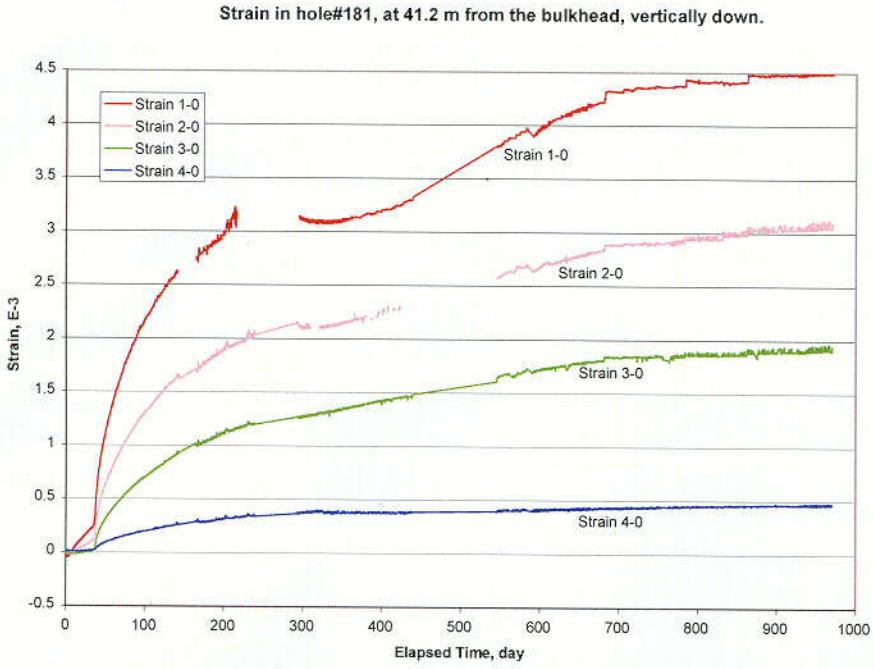

Figure 116. The strain in borehole #181, which is at 41.1 m from the bulkhead, vertically down.

C21

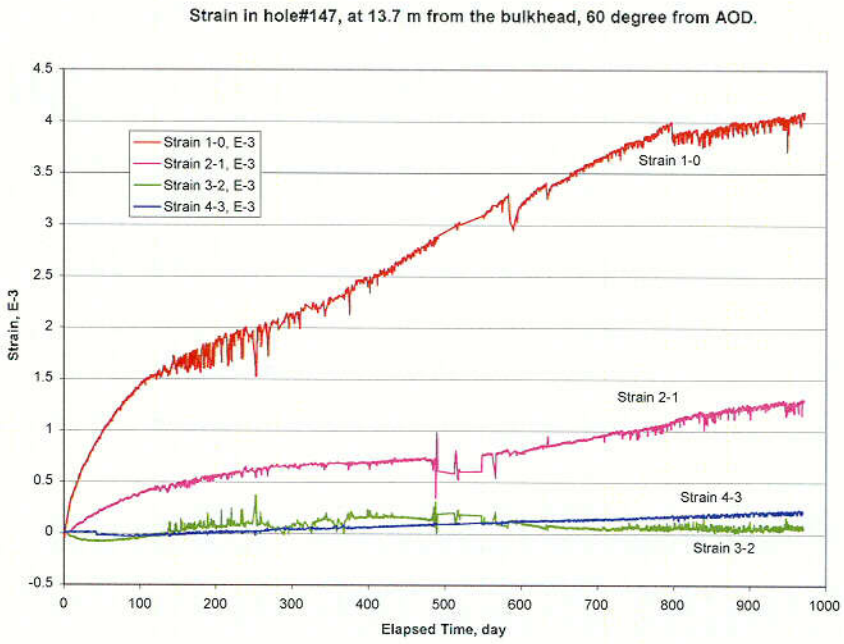

Figure 117. The strains in borehole #147, which is at 13.7 m from the bulkhead. This borehole is 60 degree away from the AOD.

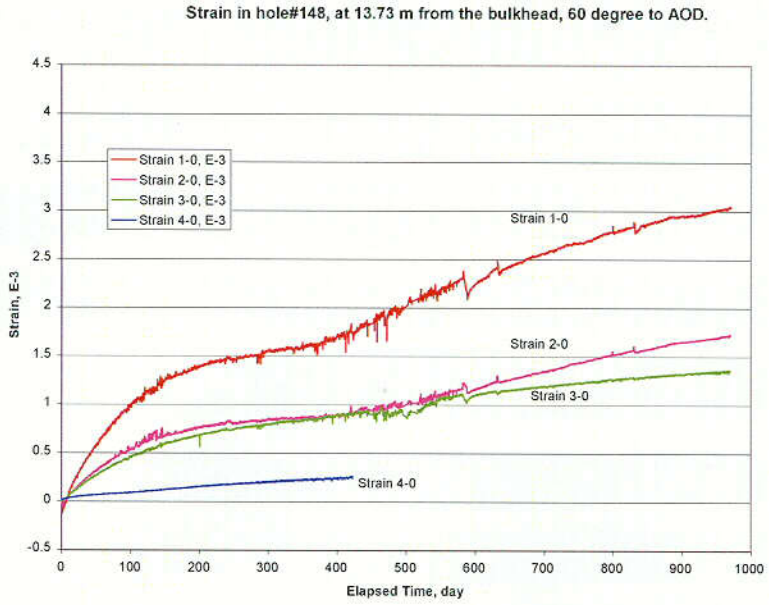

Figure 118. The strains in borehole #148, which is at 13.7 m from the bulkhead. This borehole is 60 degree to ward the AOD.

C22

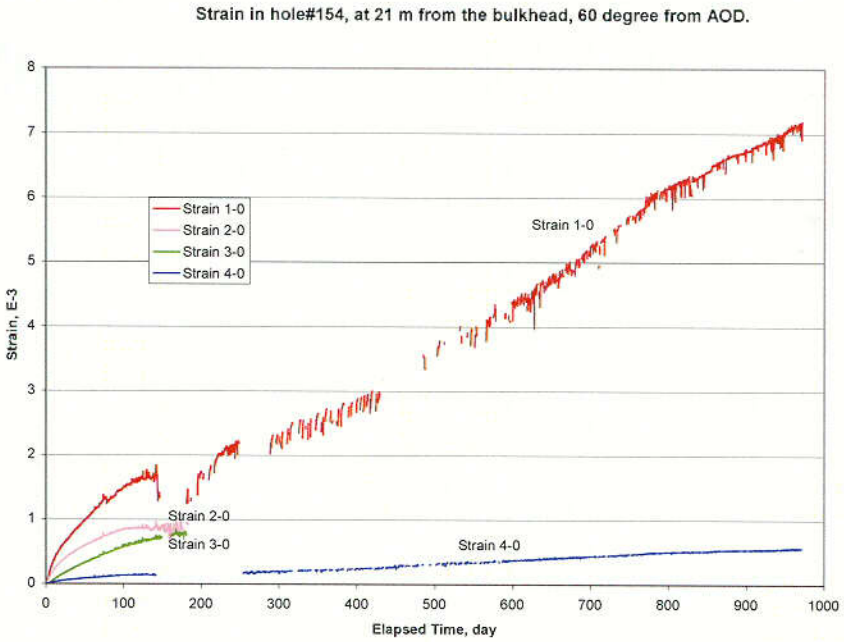

Figure 119. The strains in borehole #154, which is at 21 m from the bulkhead, 60 degree away from the AOD.

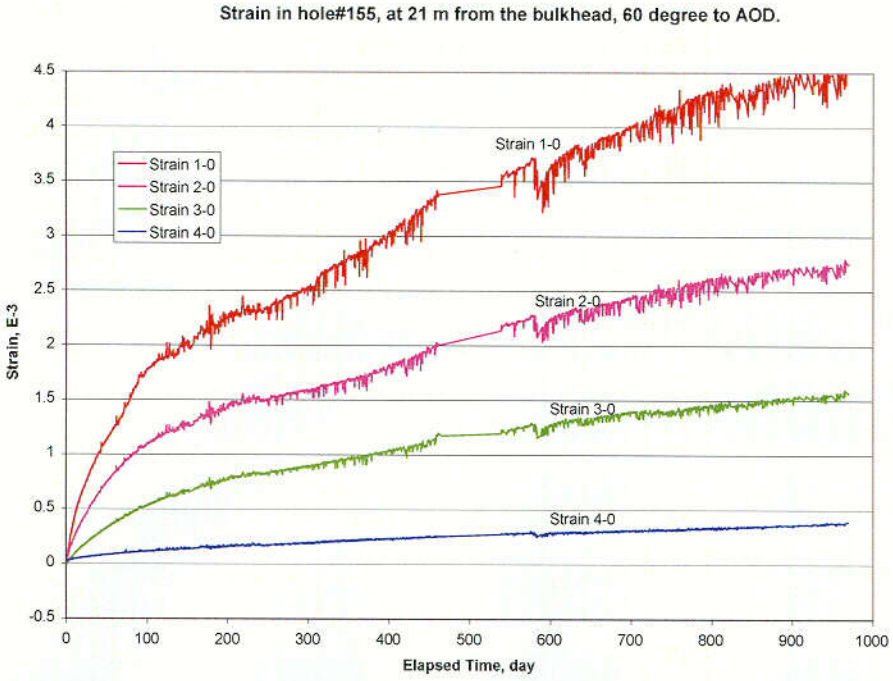

Figure 120. The strains in borehole #155, which is at 21 m from the bulkhead, 60 degree toward the AOD.

C23

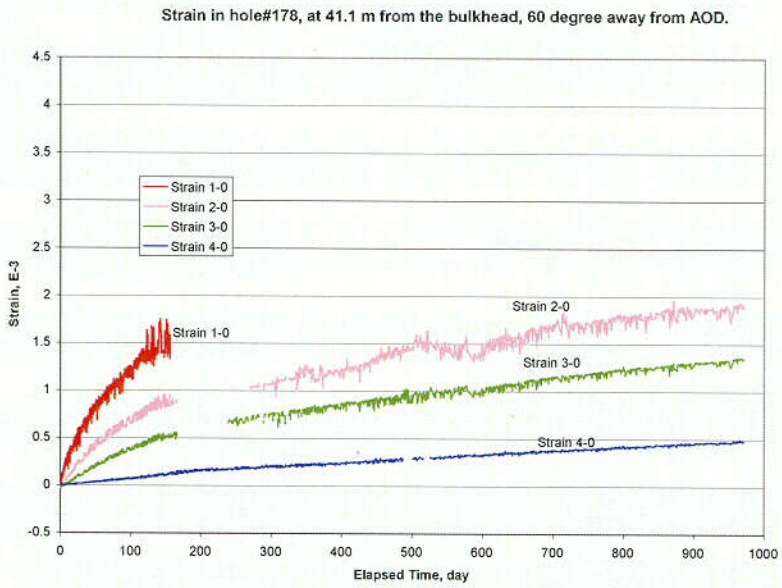

Figure 121. The strains in borehole #178, which is at 41.1 m from the bulkhead, 60 degree away from the AOD.

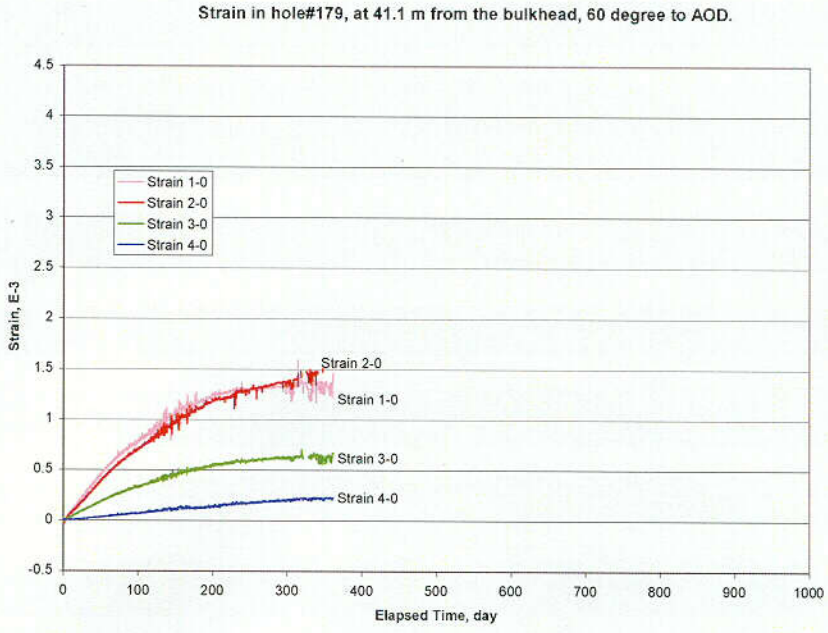

Figure 122. The strains in borehole #179, which is at 41.1 m from the bulkhead, 60 degree toward the AOD.

C24

5.3 THM Model Validation: Integrated Assessment of Measured and Predicted Behavior

This section presents results of coupled thermal-hydrological-mechanical (THM) simulations of two field-scale tests that are part of the thermal testing program being conducted by the Yucca Mountain Site Characterization Project. The two tests analyzed are the Drift Scale Test (DST) which is sited in an alcove of the Exploratory Studies Facility at Yucca Mountain, Nevada, and the Large Block Test (LBT) which is sited at Fran Ridge, near Yucca Mountain, Nevada. Both of these tests were designed to investigate coupled thermal-mechanical-hydrological-chemical (TMHC) behavior in a fractured, densely welded ash-flow tuff.

The geomechanical response of the rock mass forming the DST and the LBT is analyzed using a coupled THM model. A coupled model for analysis of the DST and LBT has been formulated by linking the 3DEC distinct element code for thermal-mechanical analysis and the NUFT finite element code for thermal-hydrologic analysis. The TH model (NUFT) computes temperatures at preselected times using a model that extends from the surface to the water table. The temperatures computed by NUFT are input to 3DEC, which then computes stresses and deformations. The distinct element method was chosen to permit the inclusion of discrete fractures and explicit modeling of fracture deformations. Shear deformations and normal mode opening of fractures are expected to increase fracture permeability and thereby alter thermal-hydrologic behavior in these tests. We have collected fracture data for both the DST and the LBT and have used these data in the formulation of the test model. This paper presents a brief discussion of the model formulation, along with comparison of simulated and observed deformations at selected locations within the tests.

5.3.1 Drift Scale Test

Test Description and Model Development

The drift-scale heater test, the DST, is being conducted in an alcove of the Exploratory Studies Facility (ESF) at Yucca Mountain, Nevada. The DST is a large-scale, long-term thermal test designed to investigate coupled thermal-mechanical-hydrological-chemical behavior in a fractured, welded tuff rock mass.

The general layout of the DST is shown in Figure 123. The heated drift (HD) is a 5-m-diameter drift approximately 60 m long. Access to the HD from the ESF is gained through the Access Observation Drift (AOD) and a connecting drift. Heat is being supplied to the rock mass forming the DST via nine electric canister heaters located in the HD, and wing heaters placed in 50 boreholes oriented perpendicular to the HD. These wing heater boreholes are spaced at 2-m intervals along each rib of the HD. The wing heaters extend into the rock approximately 11 m from the rib. Together, these heaters are providing approximately 180 kW of power to heat an approximately planar region of rock that is approximately 50 m long and 27 m wide. The test plan (CRWMS M&O 1997) calls for 4 years of heating followed by a 4-year cool-down period. The heating portion of the DST was started in December 1997, and the target drift wall temperature of 200°C was reached in summer 2000. Deformation of the rock mass is being monitored with an array of multiple-point borehole extensometer (MPBX) systems. Locations of

the MPBX boreholes are shown in Figure 123. These boreholes represent only a small fraction of the boreholes drilled into the DST for emplacement of various types of instrumentation that enable temperature, geophysical, hydrological, and chemical measurements.

The THM model for the DST incorporates the actual geometry of excavations forming the DST. The model was run in two different modes; a "basecase" model that included fractures, and a simple "continuum" model. For the continuum case, no fractures were included and 3DEC was used to simulate the DST as one large, uniform isotropic block of rock. Fractures included in the basecase model are derived from a data set of fractures mapped in the DST block. Temperatures are from TH simulations of the DST. The drift dimensions and the sensor and borehole locations were taken from CRWMS M&O 1998. Specifics of the model formulation are discussed below. DTN information for temperatures, MPBX data, fractures, and other information is listed in Table 4. The input and output files for the Drift Scale Test model validation simulations have been submitted to the TDMS (DTN: LL010700123123.013).

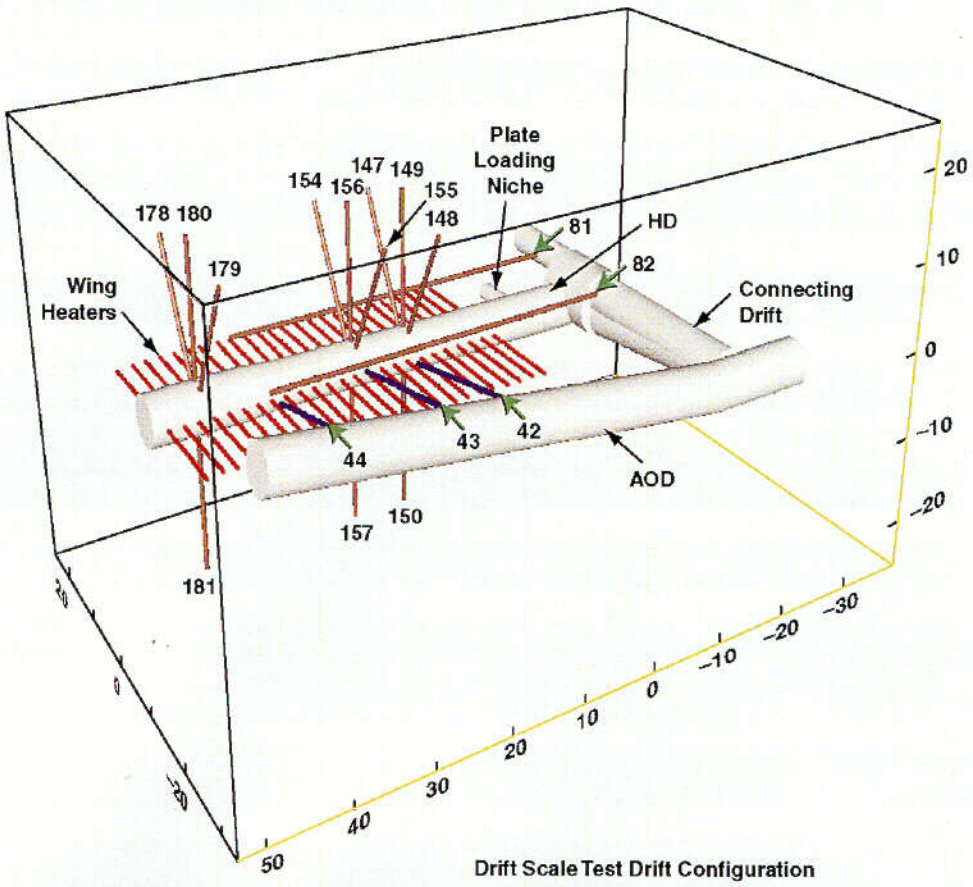

Source: Borehole locations are from *Drift Scale Test As-Built Report* (CRWMS M&O 1998).

Figure 123. Layout of the Drift Scale Test. Numbered boreholes are those containing MPBX instrumentation.

C25

Table 4. DTNs for Model Validation

Description	Start Date	End Date	Data Tracking Number
Large Block Test Data			
Fracture Sets	02/97	02/98	LL981004604243.024
Temperatures	02/97	09/98	LL980918904244.074
MPBX Displacements	02/97	09/98	LL980919404244.076
	02/97	02/98	LL981004604243.024
Single Heater Test Data			
Temperatures	08/96	11/97	SNF35110695001.008
	12/97	01/98	SNF35110695001.009
MPBX Displacements	08/96	11/97	SNF35110695001.008
	12/97	01/98	SNF35110695001.009
Drift Scale Test Data			
Temperatures	01/97	03/98	LL981105604243.025
	12/97	02/98	LL980601704244.062
	11/97	05/98	MO9807DSTSET01.000
	06/98	08/98	MO9810DSTSET02.000
	09/98	05/99	MO9906DSTSET03.000
	06/99	10/99	MO0001SEPDSTPC.000
	11/99	05/00	MO0007SEPDSTPC.001
Smoothed MPBX Displacements	12/97	07/00	SN0106F3912298.028
Fracture Data	NA	04/00	LL000116204243.035

Temperatures. Temperature inputs for the model validation simulations were taken from the NUFT simulations of the DST described in the *Thermal Tests Thermal-Hydrological Analyses/Model Report* (CRWMS M&O 2000, Section 6.2.3, p. 63). Temperatures from these simulations were regridded using the EarthVision program as follows. A three-dimensional temperature field for the region simulated by the large-scale mechanical model was produced from the two-dimensional NUFT temperature field in two steps: the NUFT temperature field was first reflected across a vertical plane through the center of the drift, then the temperatures were repeatedly replicated in the direction along the drift axis to form a 3D array.

Temperatures from the LDTH model and their coordinates were input into EarthVision along with an array of gridpoints generated by 3DEC for both the inner and outer regions at each calculation time. EarthVision performed a three-dimensional interpolation of the 3D LDTH model temperatures to provide an interpolated temperature for each calculation time at each of the 3DEC model gridpoints. The gridpoint temperatures were then input into 3DEC as a separate input file for each calculation time.

Temperatures were input at times of 1, 5, 10, 20, 30, 40, 60, 100, 180, 365, and 545 days after the start of heating. These times were selected to capture the initial thermal response of the rock to heating as well as the longer-term steady evolution of the temperature field. Figure 124 shows perspective plots of the temperature field at times selected for simulations.

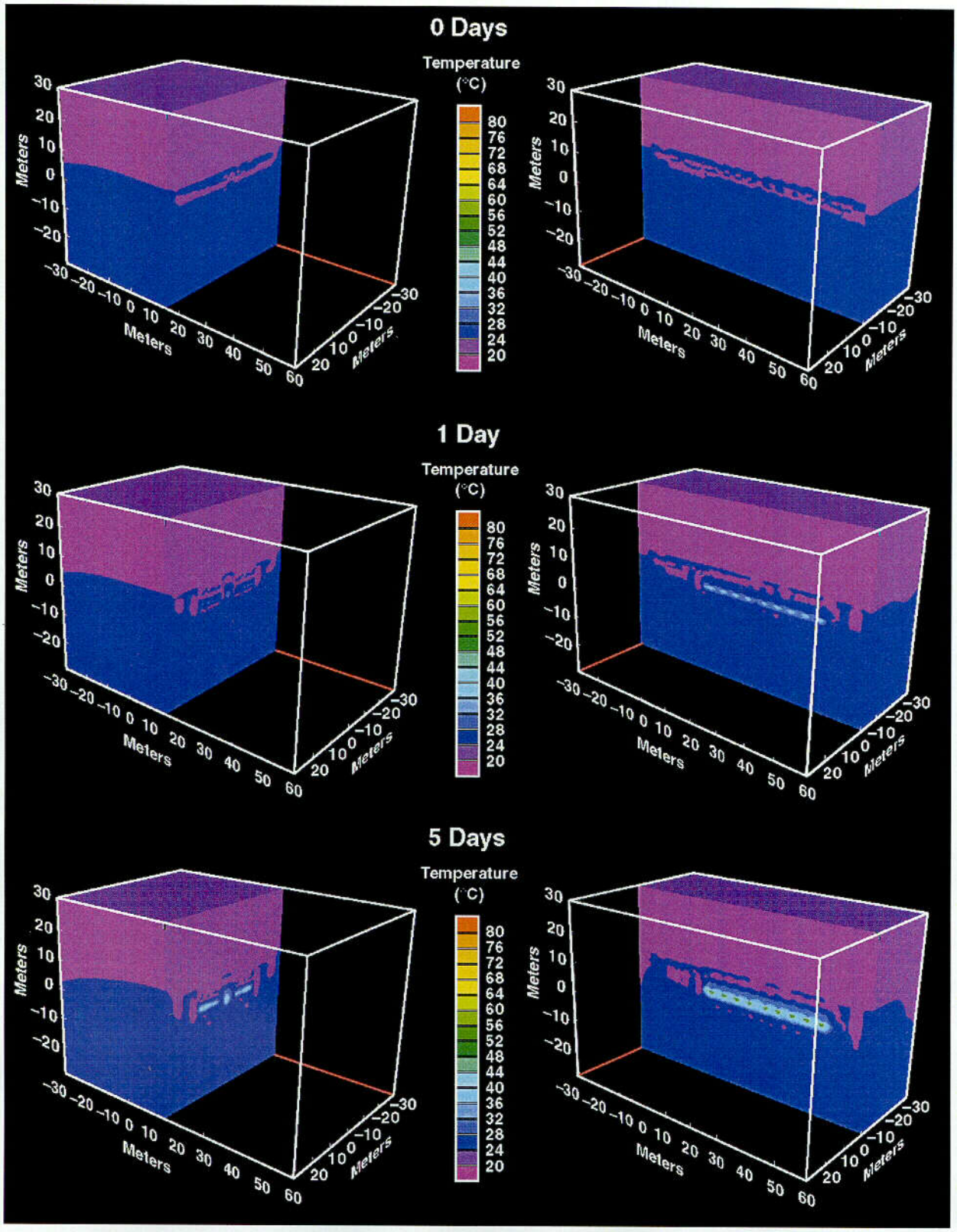

Figure 124. Perspective Plots of the Temperature Field at Times Selected for Simulations.

C26

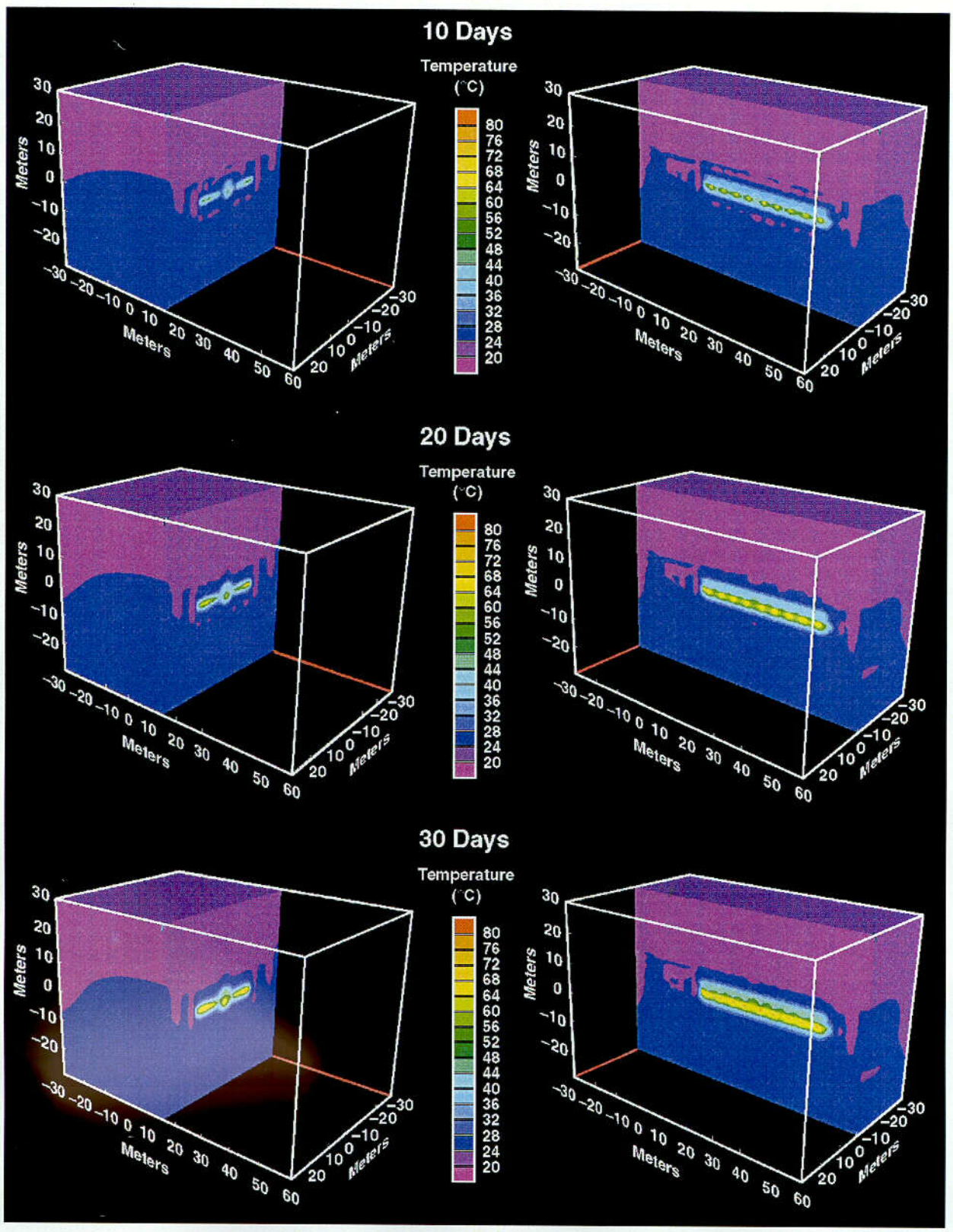

Figure124 (Continued).

C27

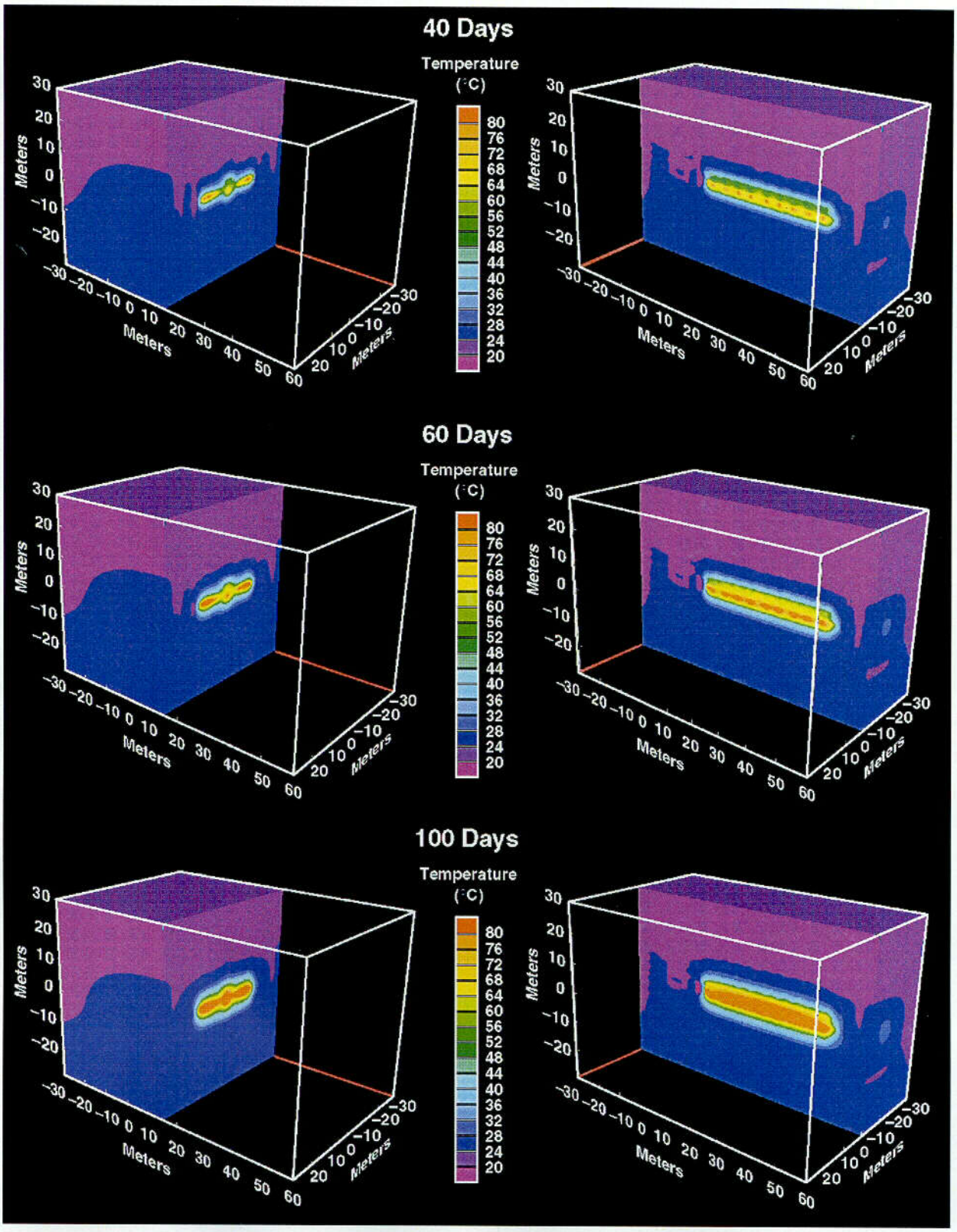

Figure 124 (Continued).

C28

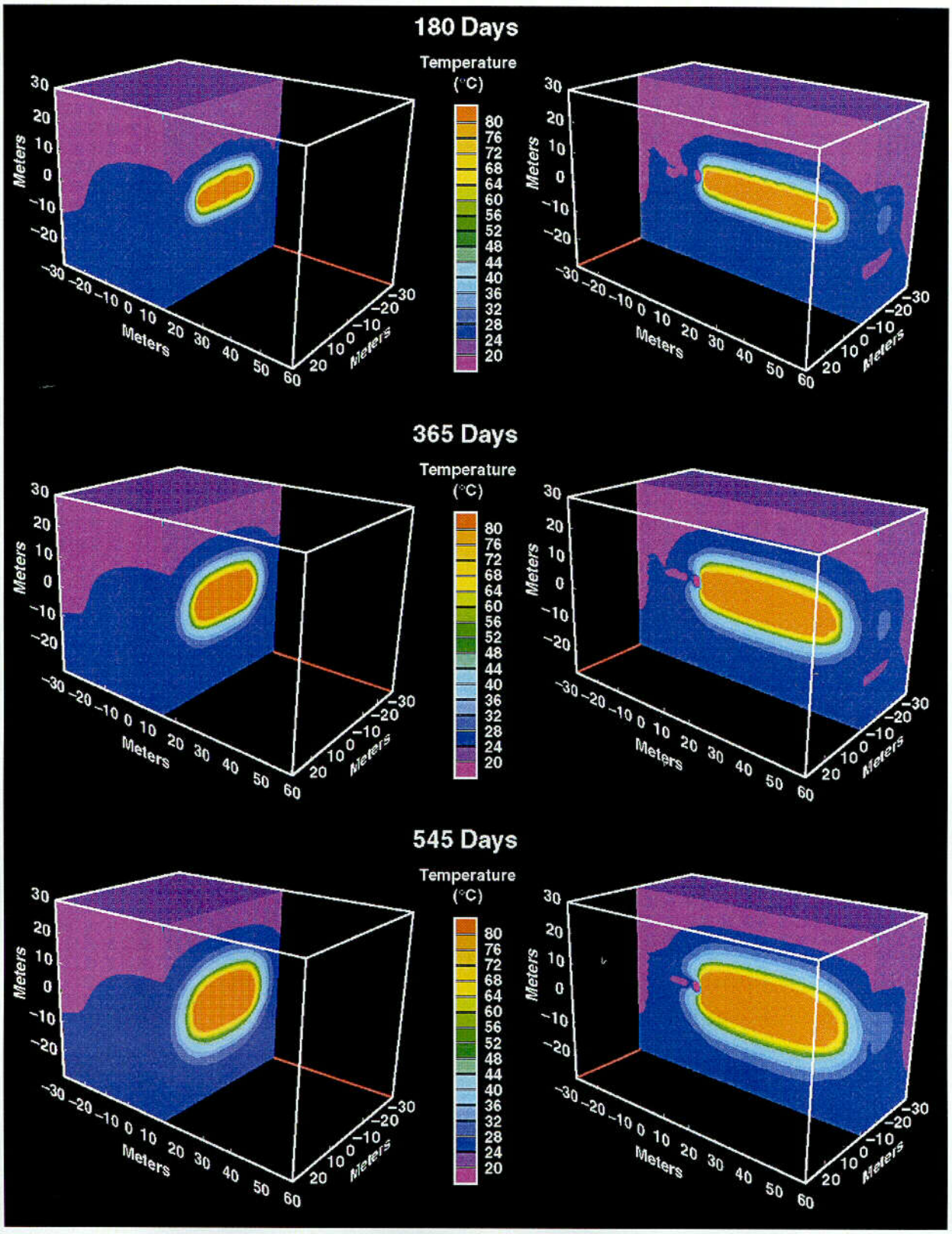

Figure 124 (Continued).

C29

Fractures. Data on fractures in the rock mass forming the DST were obtained by analyzing video logs for approximately 30 of the boreholes drilled into the DST (DTN: LL000116204243.035). Individual fractures were identified from the logs and their locations and orientations were noted. Each fracture was assigned a qualitative designation of minor, moderate, or major. Major fractures were identified as those having significant aperture, secondary mineralization, alteration haloes, and local evidence of displacement. Fracture zones are also considered to be "major" fractures. The fractures used are listed in Table 5 and the spatial locations and orientations of the major fractures used in this study are shown in Figure 125. The figure shows a higher density of fractures in the region approximately 20 m from the bulkhead of the HD and between the HD and the AOD. The DTN for the fracture data is listed in Table 4.

Table 5. Fractures Listed by XYZ Location, Taken from DTN: LL000116204243.035

Fracture No.	Dip Direction (°)	Dip Angle (°)	X coordinate (m)	Y coordinate (m)	Z coordinate (m)
1	199	75	–21.40	–8.26	4.11
2	86	83	–12.86	–10.11	–3.93
3	122	61	–13.52	–9.70	–1.38
4	28	13	–4.91	–8.32	5.57
5	51	6	–1.87	–6.60	6.35
6	9	31	–25.79	–8.20	1.57
7	21	62	–9.70	–6.54	5.51
8	20	84	–3.32	–8.33	5.71
9	22	68	–1.57	–8.28	16.26
10	20	82	–3.59	–6.59	6.17
11	20	84	–15.50	–8.28	4.63
12	124	81	–22.44	–8.17	0.58
13	100	88	–16.81	–8.13	–1.08

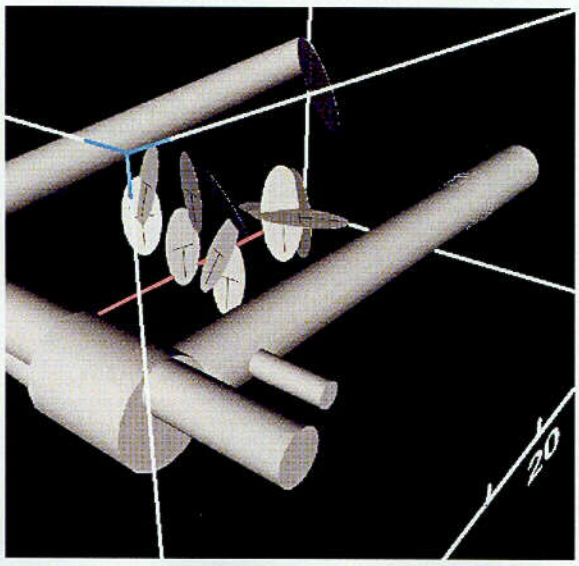

Figure 125. Spatial Locations and Orientations of the Major Fractures Used in the Basecase Analysis.

C30

Model Geometry. The geometry of the simulation is as follows. Excavations representing the AOD, Cross Drift, Heated Drift, and Plate Loading Niche were excavated from a simulated block of rock with dimensions 110 m × 55 m × 50 m. Then fractures listed in Table 5 were introduced. These fractures are allowed to extend to the edges of the model domain. The model domain with fractures included is shown in Figure 126. Excavations are shown in Figure 127.

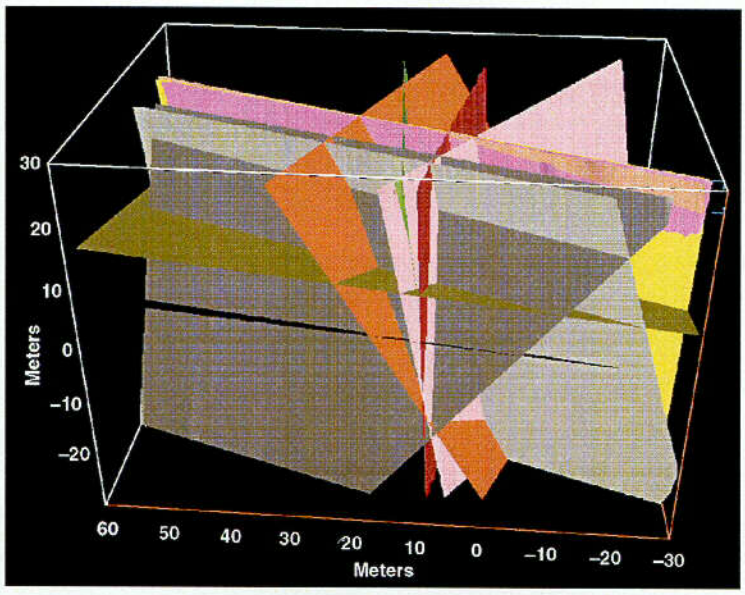

Figure 126. Model Domain with Fractures Included, Used for Basecase Simulation.

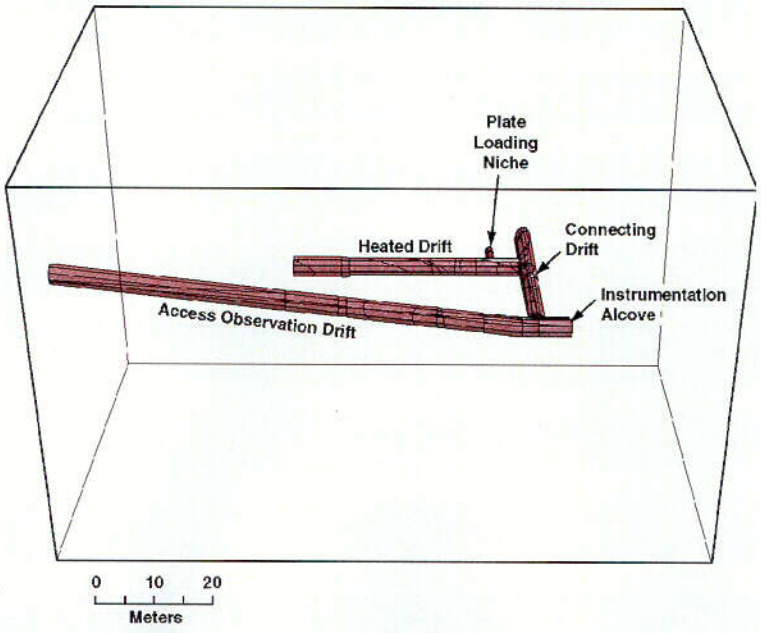

Figure 127. Excavations of Drifts and Niches Associated with the DST from the Model Domain.

C31

Boundary Conditions. Boundary conditions were applied to the simulated rock mass as follows. The base of the model was considered to be a roller boundary so that no vertical displacement was allowed. However, horizontal displacements were allowed.

The vertical sides and top of the rock mass were considered stress boundaries, and an in situ stress condition was applied with a vertical stress of 9.7 MPa and a horizontal stress of 4.85 MPa (Schelling 1989). Stress gradients were 0.023 MPa per meter of depth for vertical stresses and 0.0115 MPa per meter of depth for horizontal stresses. The stress boundary is considered appropriate as rock surrounding the DST is at ambient conditions.

Rock Properties. Both the DST and LBT are sited in the middle nonlithophysal unit of the Topopah Spring Tuff. Input parameters for the TM emplacement drift base case are provided in Table 6 and are the same as those used for the emplacement drift analysis presented in CRWMS M&O 2001. Calculated or assumed parameters are listed in Table 7. Bulk and shear modulus can be calculated from the elastic modulus (E) and Poisson's ratio (ν) as

$$K = E/(3(1-(2\nu))) \quad \text{and} \quad G = E/(2(1+\nu))$$

(Jaeger and Cook 1979), and values are given in Table 7. The input values for joint normal stiffness and joint shear stiffness assume a joint spacing of 1 m and were calculated with a relationship given in the 3DEC User's Guide (Itasca 1998, Section 3, p. 94). The joint normal stiffness calculation used an intact rock elastic modulus of 33.03 GPa (DTN: MO9911SEPGRP34.000, Table 8) and a rock mass elastic modulus of 24.71 GPa (DTN: MO9911SEPGRP34.000, Table 10). Shear moduli for the joint shear stiffness calculation were obtained from the above elastic moduli and a Poisson's ratio of 0.21 (DTN: MO9911SEPGRP34.000, Table 11). The other input parameter values were taken directly from the Technical Data Management System. The input parameters are considered appropriate because they are derived from field and laboratory measurements of the host rock physical properties, or are based on EDA II design parameters.

Table 6. Input Parameters and Data Tracking Numbers

Item No.	Description	Value	Units	Data Tracking Number
	Matrix Properties			
1	Dry Bulk Density	2270	kg/m^3	MO0003SEPDRDDA.000
2	Intact Rock Elasticity Modulus	33.03	GPa	MO9911SEPGRP34.000
3	Rock Mass Elasticity Modulus	24.71	GPa	MO9911SEPGRP34.000
4	Poisson's Ratio	0.21	none	MO9911SEPGRP34.000
	Joint Properties			
5	Joint Friction	41	deg	MO0010RDDAAMRR.002
6	Joint Cohesion	0.09	MPa	MO9911SEPGRP34.000
	Thermal Properties			
7	Thermal Conductivity	2.33	W/m-K	MO9911SEPGRP34.000
8	Thermal Expansion Coefficient	9.73E-6	deg C^{-1}	SNL22100196001.001
	Input Temperatures			
9	Input Temperatures	various	deg C	LL000114004242.090

Table 7. Calculated or Assumed Model Parameters

Description	Value	Units
Matrix Properties		
Rock Mass Bulk Modulus	14.2	GPa
Rock Mass Shear Modulus	10.2	GPa
Joint Properties		
Joint Tensile Strength	0	MPa
Joint Normal Stiffness	98.1	MPa/mm
Joint Shear Stiffness	40.5	MPa/mm
Joint Dilation Angle	29	deg
Initial Joint Aperture	0.098	mm
Boundary and In Situ Stresses		
In Situ Stress (280 m depth)	5.54	MPa
Vertical Stress Gradient	0.021	MPa/m

Results for Drift Scale Test

This section presents results of the model predictions of displacement for MPBX systems used in the DST, and compares the predicted displacements with those observed during the first 545 days of heating in the DST. For this analysis, comparisons are made for MPBX data collected for 10 of the 17 MPBX boreholes in the DST. The boreholes and anchors used are listed in Table 8.

Moreover, in the Qualitative Results discussion below, model predictions at a series of times are compared with observations. This is done for the deepest anchor in the MPBX boreholes listed in Table 8. The deepest anchor was chosen as it best represents the rock mass behavior. Note that for boreholes 42 and 43 anchor 1 is the deepest, while for the remainder of the boreholes anchor 6 is the deepest, i.e., farthest from the borehole collar.

Table 8. List of MPBX Anchors Simulated for DST

Hole	Anchor No.					
42	1	2	3	4	5	6
43	1	2	3	4	5	6
81	1	2	3	4	5	6
82	1	2	3	4	5	6
147	1	2	3	4		
148	1	2	3	4		
149			3	4		
150		2		4		
156				4		
180				4		

Qualitative Results. ***Simulation of Mine-by***—Prior to the excavation of the HD three boreholes were drilled from the AOD perpendicular to the planned location of the HD. These boreholes (42, 43, and 44) were instrumented with MPBX systems and deformations were recorded during the excavation of the HD. The borehole response due to the excavation was simulated using the DSDE model, and can be used to calibrate the bulk and shear moduli of the rock mass in the simulation.

The excavation of the HD was simulated by excavating the entire length of the HD at one time. Thus the time history of the HD excavation was not simulated, but the effect of the excavation on the rock in boreholes 42 and 43 was determined. Borehole 44 was not used in this analysis as the data for this borehole were judged to be of poor quality.

The deformation of the deepest anchors in boreholes 42 and 43 was simulated and the resulting total deformation is listed for the simulation in Table 9 along with total deformation as measured by the MPBX systems. The total deformation is shown graphically for boreholes 42 and 43 in Figure 128. This figure shows that the prediction overestimates the observed deformation by 45% in borehole 42, and by 32% in borehole 43. Thus both estimates are within an order of magnitude of the observations.

Table 9. Deformation Due to Mine-by of HD

Borehole	Anchor 6 max (mm)	Predicted deformation (mm)
42	2.4	3.5
43	3.1	4.1

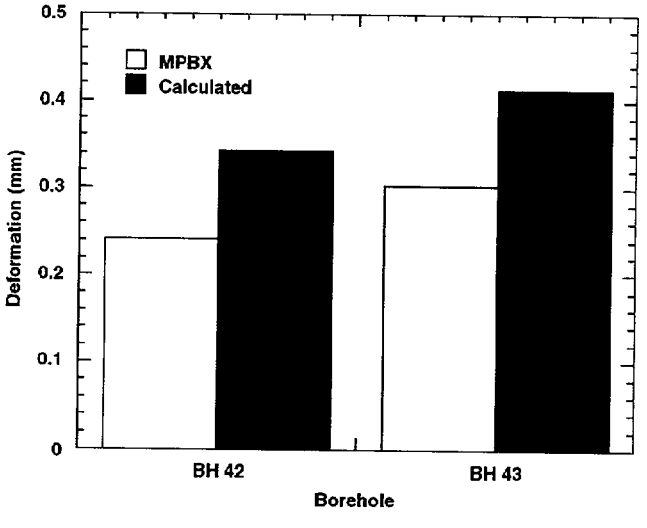

Figure 128. Total Deformation for Boreholes 42 and 43 During Mine-by, Prior to Heating.